Correspondence to:
C. B. Senel,
cem.berk@observatory.be

Author Contributions:
Conceptualization: Cem Berk Senel, Orkun Temel, Özgür Karatekin
Formal analysis: Cem Berk Senel, Orkun Temel
Investigation: Cem Berk Senel, Orkun Temel, Christopher Lee, Claire E. Newman, Michael A. Mischna, Domingo Muñoz-Esparza, Hakan Sert, Özgür Karatekin
Methodology: Cem Berk Senel, Orkun Temel, Christopher Lee, Özgür Karatekin
Resources: Özgür Karatekin
Software: Cem Berk Senel, Orkun Temel, Christopher Lee, Michael A. Mischna
Supervision: Özgür Karatekin
Validation: Cem Berk Senel, Özgür Karatekin
Visualization: Cem Berk Senel, Orkun Temel, Claire E. Newman, Michael A. Mischna, Domingo Muñoz-Esparza, Hakan Sert

Interannual, Seasonal and Regional Variations in the Martian Convective Boundary Layer Derived From GCM Simulations With a Semi-Interactive Dust Transport Model

Cem Berk Senel[1] , Orkun Temel[1,2] , Christopher Lee[3,4] , Claire E. Newman[4] , Michael A. Mischna[5] , Domingo Muñoz-Esparza[6] , Hakan Sert[1], and Özgür Karatekin[1]

[1]Royal Observatory of Belgium, Reference Systems and Planetology, Brussels, Belgium, [2]KU Leuven, Institute of Astronomy, Leuven, Belgium, [3]Department of Physics, University of Toronto, Toronto, ON, Canada, [4]Aeolis Research, Pasadena, CA, USA, [5]Jet Propulsion Laboratory, California Institute of Technology, Pasadena, CA, USA, [6]National Center for Atmospheric Research, Boulder, CO, USA

Abstract We present interannual, seasonal, and regional variations in the daytime Martian convective boundary layer (CBL). Martian CBL meteorology is driven both by the effect of diurnal and seasonal cycles as well as complex Martian topography. One of the most important components of the Martian atmosphere is its dust cycle. Here, we develop a novel semi-interactive dust transport model within the MarsWRF framework, in which the dust is lifted, advected by model winds, mixed, and allowed to sediment, but is then scaled to match two-dimensional maps of the observed daily column-integrated dust opacity. This allows the vertical dust distribution and associated dust radiative heating to be controlled by model processes, while the horizontal dust distribution is constrained to follow observations. We report the impact of the dust cycle on Martian boundary layer meteorology. Enhanced dust transport lowers the global net surface heating rates, decreasing the turbulent mixing in CBL to virtually zero (within the dust storm season) and, enhances the wind shear on average by almost 50%. As a superposition of both impacts, during global dust storms (GDS) in Mars Year (MY) 25 and 34, we find that long-lasting extremely shallow daytime boundary layers can globally form as shallow as 0.5 km (but not for the less intense GDS in MY 28), unlike the 9 km deep and highly turbulent CBL formation at GDS onset and decay. Based on our GCM results, strong CBL suppression lasts as long as approximately 67 and 57 sols during GDS events in MY 25 and 34.

Plain Language Summary In recent years, thanks to the ongoing lander and rover missions, in situ observations of Martian surface processes (water, dust, and methane transport) have been attracting more attention, especially to search for the signatures of the planet's habitability. From this emerges the significance of planetary boundary layer dynamics, which is the key governor of surface exchange processes in the lowermost portion of the atmosphere. Although the current knowledge has been advancing by observing diurnal characteristics for specific locations, seasonal and year-to-year variations on a global scale are still less well comprehended. Here, we examine year-to-year, seasonal, and regional variabilities of the Martian daytime planetary boundary layer (so-called convective boundary layer governed by daytime radiative heating), assessing a decade-long general circulation model (GCM) simulation from Mars Year 24–34. Our results show that global dust storms in Mars Years 25 and 34 have profound impacts on the convective boundary layer, causing a severe surface cooling as a long-term global-darkness state, thus resulting in a global weakening in convective activity. We find that deep and highly turbulent convective boundary layers (with a depth of 9 km) convert into extremely shallow (0.5 km) boundary layers even during the daytime, as a consequence of global dust storms.

1. Introduction

The Martian planetary boundary layer (PBL) is a vital component of climate dynamics, in which its dynamics are strongly affected by radiative, microphysical, and surface processes (Petrosyan et al., 2011). It is the lowermost and likely most active layer of the atmosphere (Spiga, 2019), in which turbulent motions govern the transport of momentum, heat, dust, and volatiles between the surface and atmosphere (Michaels &

Writing – original draft: Cem Berk Senel, Orkun Temel, Özgür Karatekin
Writing – review & editing: Christopher Lee, Claire E. Newman, Michael A. Mischna, Domingo Muñoz-Esparza, Hakan Sert

Rafkin, 2004). This transport is mainly controlled by the diurnal variation in surface radiative forcing. During the daytime, surface radiative heating enhances the convective activity through buoyancy production, which is the production of turbulent convection. It results in a well-mixed boundary layer, referred to as the daytime PBL or convective boundary layer (CBL), composed of large convective eddies and deep thermal plumes (Stull, 2012). On the other hand, this process is reversed during the nighttime as the turbulent convection is suppressed by surface radiative cooling. It forms a very shallow layer on the order of tens of meters (Mason & Derbyshire, 1990; M. D. Smith et al., 2004), characterized by local shear instabilities (Banta, 2008) and intermittent turbulence (Sun et al., 2012). We see the signatures of the latter on Mars as detected by the InSight lander in Banfield et al. (2020), to be like the boundary layer formed over the polar regions on Earth (Grachev et al., 2005). Unlike the quieter mode at night, the Martian convective boundary layer becomes highly turbulent, particularly in the local afternoon, in which the depth of the CBL can rise to in excess of 10 km (above the local surface) (Hinson et al., 2008). This is one order of magnitude deeper than a typical convective boundary layer formed on Earth, which is only on the order of ~1 km (Moeng & Sullivan, 1994; Gheynani & Taylor, 2010). This implies, accordingly, a more intensified diurnal contrast between daytime and nighttime on Mars than is encountered on Earth, as a consequence of the fact that Mars has a lower atmospheric density (Larsen et al., 2002; Wilson & Hamilton, 1996) and lower surface thermal inertia (Putzig & Mellon, 2007). In addition to the intense diurnal variability, the Martian PBL exhibits seasonal and interannual changes, likely influencing the circulation dynamics and thermal composition of the atmosphere from the surface to the free atmosphere (i.e., the region above the PBL that is a stably stratified layer preventing the further growth of the PBL [Brooks & Fowler, 2012]). This variability is possibly modulated by the dust cycle on Mars (Haberle et al., 1982; Heavens et al., 2011b; Kass et al., 2020; Liu et al., 2003; Newman et al., 2002; Wolkenberg et al., 2018). In the meanwhile, the exchange of dust content between the surface and atmosphere is strongly influenced by PBL dynamics (Spiga, 2019). For instance, a stronger production of daytime turbulent convection exerted by strong radiative heating would impact the vertical dust distribution, injecting dust particles into the upper layers of the PBL (Guzewich, Talaat, et al., 2013). This process is further enhanced, locally, by the presence of dust devils (Rennó et al., 2004; Spiga et al., 2016), which is one of the two main contributors of dust lifting besides the lifting by near-surface winds (Newman & Richardson, 2015). Such an enhancement in lifting through dust devils and near-surface winds occurs in both hemispheres in local summer, as a consequence of high solar forcing and strong winds (Newman, Lee, et al., 2019). Besides, the Martian dust cycle features stronger dust events, such as regional and planet-encircling dust storms (Martin & Zurek, 1993). The latter are also known as Global Dust Storms (GDS), affecting the entire thermal and circulation structure of the planet from the lower atmosphere (Aoki et al., 2019; Basu et al., 2006) to the upper atmosphere (Fedorova et al., 2020; Liuzzi et al., 2020; Neary et al., 2020). GDS originate around southern spring equinox or summer solstice, lifting a large mass of dust and entraining it into the upper layers of the atmosphere (Montabone et al., 2020), reaching nearly 80 km during a GDS's mature phase, as observed by the Mars Climate Sounder (MCS) (Kass et al., 2020). These storms encircle the planet, sustaining the transport of dust for a long period, from weeks to months (Guzewich et al., 2019). In such a way, GDS have a profound effect on PBL dynamics (Haberle et al., 1993) because the long-term presence of a global dust storm tends to continuously attenuate the surface net radiative heating as most of the incoming sunlight is absorbed by dust particles (Spiga, 2019). Three major GDS have been observed in the last 10 Mars years. These are recorded in Mars Years (hereafter MY) 25, 28, and recently, in MY 34 (Kleinböhl et al., 2020). Moreover, the Martian PBL exhibits significant regional variabilities due to the complexity in geophysical properties of the terrain (i.e., thermal inertia and albedo) and elevation of Mars' topography. Mars, having steep mountains, deep canyons, and large impact craters, has a severe surface heterogeneity. For instance, Olympus Mons is almost 25 km in height (Milkovich et al., 2006) and Valles Marineris is a canyon that spans around 4,000 km (Fueten et al., 2005). Such extremes in Martian topography make the local PBL exhibit more irregular spatial variability, producing highly turbulent gradients in near-surface winds such as katabatic and anabatic winds that are two to three times more intense than the same winds on Earth (Spiga & Lewis, 2010). Here, the anabatic winds refer to the upslope convective winds over mountains, craters, and canyons (Newman et al., 2017), resulting in less turbulent convection at the onset of upslope winds, for example, in the center of canyons (Moores et al., 2015; Spiga & Forget, 2009). As acquired by the Navigation Cameras (Navcams) onboard the Mars Science Laboratory (MSL), rover assisted by mesoscale simulations, Moores et al. (2015) found observational evidence for a severe suppression in the CBL along northern Gale crater in which fewer dust devils appear. This suppression was quantified with

mesoscale simulations over Gale crater (Tyler & Barnes, 2013), showing CBL depth as shallow as 1–2 km within the crater unlike the exterior plains for which the CBL could reach depths of 10 km. More recently, Guzewich et al. (2017) determined the annual variation of the diurnal peak in CBL depth from MCS profiles, ranging between 2 and 5.5 km within Gale crater due to the suppression by daytime upslope winds. Newman, Kahanpää, et al. (2019) use MarsWRF to show that, while the CBL is suppressed in the crater trench for about half the Mars year (including the landing period, $L_s \sim 150°$), the peak CBL depth is actually predicted to be enhanced in the crater trench, compared to Mt. Sharp, during southern summer and surrounding period. Newman, Kahanpää, et al. (2019) also suggest that it is the sensible heat flux, based on the near-surface temperature gradient and wind stress, not the CBL depth, that has the biggest impact on finding more dust devils as one moves up the slopes, while the CBL depth appears to have a larger impact on seasonal variations. On the other hand, the depth of the CBL on Mars is also influenced by the elevation of the topography (Pätzold et al., 2016). Hinson et al. (2008) determined the CBL depth from radio occultation (RO) measurements by the Mars Express (MEX) orbiter with a horizontal resolution of 400 km (i.e., nearly 7° resolution in the longitudinal direction along the equator). These radio occultations cover the latitudes between 15°S and 54°N at 38 locations during the northern midspring of MY 27 ($L_s = 34.7° - 69.2°$). By these experiments, they found a significant correlation between the terrain elevation and CBL depth with shallow CBL formations in Utopia and Amazonis Planitia (e.g., 4–6 km) becoming deeper at higher terrains, for instance around Syrtis Major and Tharsis Montes (e.g., 8–10 km). Hinson et al. (2019) later relate this dependence to the surface potential temperature, combining radio occultations with infrared sounding. Their results indicate that the CBL depth exhibits high spatial variability ranging from a few kilometers up to in excess of 9 km between lower and higher terrains, while a gradual variability appears in terms of seasonal change (e.g., ~1 km increase in CBL depth) as these measurements are collected during the northern midspring and late winter of MY 27 as well as in the early spring of MY 28 (in early to late afternoon at 118 locations). To date, studies addressing the Martian planetary boundary layer have presented crucial insights into its depth (Hinson et al., 2008, 2019), turbulent circulations (Paton et al., 2018), thermal structure (Hamilton et al., 2014), and dust activity (Banfield et al., 2020; Perrin et al., 2020), inferred from either in-situ or orbiting satellite observations. Using ground-based observations in combination with the similarity theory, the Martian PBL depth was estimated at the Viking and Phoenix landing sites in Martínez et al. (2009). Meanwhile, there have been numerical efforts using turbulence-resolving large-eddy simulations (LES) at microscale grid resolutions (Michaels & Rafkin, 2004; Spiga & Lewis, 2010; Temel et al., 2020), mesoscale simulations on regional domains (Fonseca et al., 2018; Guzewich et al., 2017; Tyler & Barnes, 2013), and the general circulation model (GCM) simulations of CBL at planetary scales (Colaïtis et al., 2013). However, all these efforts are limited to either specific locations or particular time episodes in a given season or year, due to the observational limitations or high computational demand of the numerical simulations. Therefore, in the present study, our aim is to conduct a comprehensive investigation of the spatial and temporal variability of the Martian CBL derived from GCM simulations. More specifically, this variability is examined on interannual, seasonal, and regional spatiotemporal scales over the last decade of Martian Years (from MY24 to MY34). Thus, our investigation also deals with dust-CBL interactions, while GDS encircle the planet. It is worth noting that the current study is solely devoted to the daytime convective boundary layer. The reason is that proper modeling of the nighttime PBL, that is, ranging between the order of tens to hundreds of meters in depth (Davy et al., 2010; Spiga, 2019), is likely to require turbulence resolving large-eddy simulations due to the presence of smaller eddy sizes as well as the complexity of stably stratified intermittent turbulence (Kosović & Curry, 2000; Senel et al., 2019; Temel et al., 2020). In Section 2, we present the methodology, describing the MarsWRF GCM (Richardson et al., 2007) and details of the physical models used. We also validate the model's dust processes by comparing the simulated dust distribution to that observed by MCS. Section 3 describes the GCM experiments giving computational details, then the results in terms of interannual, seasonal, and regional variations in the Martian CBL, and a comparison between the modeled CBL depths by comparing with MEX radio occultation (RO) measurements. Finally, Section 4 presents our conclusions and discussions.

2. Methods

2.1. Description of the MarsWRF General Circulation Model

To perform GCM simulations, we utilize the MarsWRF model, which is the Mars version of the planetWRF model (Newman & Richardson, 2015; Richardson et al., 2007; Toigo et al., 2012) based upon the terrestrial Weather Research and Forecast (WRF) model (Skamarock et al., 2008). In MarsWRF, we use the two-stream correlated k-distribution scheme for the shortwave and longwave radiative transfer (Mischna et al., 2012). To model the turbulent mixing of momentum, heat, dust, and aerosols between the surface and atmosphere, we use our recent implementation of a Mars-specific PBL scheme (Temel et al., 2020), using a local and 1.5-order turbulence kinetic energy (TKE) closure scheme, in which the nonlocal transport of buoyant plumes is treated based on the scheme presented in Therry and Lacarrère (1983). Our model incorporates a generic formulation for the mixing length scale in Mars-specific conditions over a wide range of convective instabilities. For the physical description and its performance compared to a terrestrial scheme with respect to MEX radio occultation observations (Hinson et al., 2008) and near-surface wind measurements from the InSight lander (Banfield et al., 2020), the reader is referred to Temel et al. (2020). The MarsWRF model has also been widely validated against remote sensing and in situ pressure and temperature observations (Guo et al., 2009; Newman & Richardson, 2015; Temel et al., 2019; Toigo et al., 2012). The vertical exchange of momentum, heat, and tracers at the surface is treated by the MarsWRF implementation of the revised MM5 scheme (Jiménez & Dudhia, 2012). Moreover, surface properties of the MarsWRF model, such as the topography, albedo, emissivity, and thermal inertia are acquired from the data sets of the Mars Orbiter Laser Altimeter (MOLA) (D. E. Smith et al., 2001) and Thermal Emission Spectrometer (TES) (Christensen et al., 2004) observations, where the details are presented in Richardson et al. (2007).

2.2. Semi-Interactive Dust Transport Scheme

The dust cycle is the most profound driver of the Martian climate; thus, capturing the time-evolving dust distribution correctly is extremely important for simulating a realistic climate. One approach is fully interactive dust modeling (Lee et al., 2018; Newman & Richardson, 2015) in which the dust transport is freely sustained without any observation-based constraints. This way would reproduce the dust cycle realistically, even when there are no observational data to guide the GCM. However, it brings limitations in properly predicting the onset time, period, intensity, and location of dust storms, in comparison with observations. To handle this incompatibility, recently, Newman, Lee, et al. (2019) made an initial assessment of a GCM simulation, including orbit-spin coupling on Mars. Even though the coupling term acceleration leads to an increase in the interannual variability of global dust storms, further refinement is still needed to capture the onset and size of global dust storms consistently.

As yet, no Mars GCM can spontaneously generate all types of observed dust storms (in terms of onset timing, location, evolution, etc.), let alone the occurrence of a particular type and size of large dust storm in the Mars year it was observed. Attempts to improve this are ongoing and include considering the limited availability of surface dust where the surface dust abundance is imposed as finite unlike an infinite dust source (Newman & Richardson, 2015), orbit-spin coupling (Newman, Lee, et al., 2019), and coupling of the dust and water ice cycles (Kahre et al., 2011, 2015; Lee et al., 2018; Madeleine et al., 2011, 2012; Navarro et al., 2014). But, it is necessary to guide GCMs using observations in some way if the impact of dust storms in a given Mars year is to be as realistic as possible. Possible approaches include: prescribing a 2D dust distribution based on 2D dust observations and using a modified Conrath profile (hereafter referred to as a prescribed dust scheme) to determine the vertical variation (Conrath, 1975; Forget et al., 1999); prescribing the 3D dust distribution using TES limb and nadir dust observations (Guzewich, Toigo, et al., 2013); data assimilation of observed temperatures or radiances (Greybush et al., 2012; Lee et al., 2011; Lewis et al., 1999); prescribing dust lifting based on observations (Bertrand et al., 2020; Kahre et al., 2009); and just as the present work, the semi-interactive scheme in Madeleine et al. (2011) involves rescaling the dust column based on opacity maps. It is worth noting that the semi-interactive approach differs from models in which dust is not transported in the atmosphere. In such models (e.g., the prescribed dust scheme), the vertical distribution of dust must be prescribed assuming a spatially uniform dust distribution, such that the dust opacity monotonically decreases with altitude. Nevertheless, such a prescribed dust scheme is unable to reproduce

well the enhanced dust layers at high altitudes, that is, 15–25 km, over the tropics as observed from the MCS (Heavens et al., 2011a, 2011b) or the detached dust layers due to rocket dust storms (Spiga et al., 2013; Wang et al., 2018). This motivates our approach of allowing dust to be advected by model winds, mixed by turbulent processes, and sedimented out.

To accomplish this, we adapt the existing dust transport scheme of MarsWRF (i.e., a two-moment dust transport scheme) by Lee et al. (2018) to a semi-interactive mode. The original scheme treats the atmospheric dust transport by means of a two-moment approach based on the terrestrial Morrison and Gettelman (2008) microphysics scheme. The two-moment framework of Lee et al. (2018) enables us to transport the dust advecting and diffusing in the atmosphere as two independent tracers: the mass density (q) and number density (N) of dust, where the dust particles are considered to follow a gamma function (Lee et al., 2018). The original scheme treats these tracers as $q = \frac{\pi \rho_p}{6} M_3$ and $N = M_0$, where ρ_p is the dust particle density and M_p denotes the pth-order moment of the gamma size-distribution as

$$M_p = \int_0^\infty D^p N(D) = \frac{N_0}{\lambda^{\mu+p+1}} \Gamma(\mu + p + 1) \tag{1}$$

where $N(D)$ is the gamma distribution of number density as a function of the particle diameter, D. In Equation 1, Γ refers to the integral of the gamma function in terms of intercept (N_0), shape (μ), and slope (λ) parameters as described in Lee et al. (2018). As the gamma size-distribution requires the value of μ, we set $\mu = 1$ following Lee et al. (2018), leading to a corresponding value for the effective variance of the gamma size-distribution, that is, such that $\nu_{eff} = (\mu + 3)^{-1} = 0.25$, which satisfies the range ($0.2 < \nu_{eff} < 0.8$) given in Wolff et al. (2006).

The two tracers in the two-moment framework of Lee et al. (2018), that is, q and N, are related as

$$q = N \frac{4\pi \rho_p r_{eff}^3}{3} \frac{(\mu + 2)(\mu + 1)}{(\mu + 3)^2} \tag{2}$$

in terms of the dust effective radius of the gamma-size distribution, $r_{eff} = M_3/2M_2 = (\mu + 3)/(2\lambda)$, where the initial value of r_{eff} is set to 2 μm as in Lee et al. (2018).

After having the mass density of dust, q, or, alternatively, the dust mixing ratio, in Equation 2, the distribution of the dust optical depth field, τ_d, is computed following Forget et al. (1999) and Wang et al. (2018).

$$d\tau_{d,si} = \frac{3}{4} \frac{Q_{ext,\lambda} q}{\rho_p r_{eff} g} dp \tag{3}$$

where $\rho_p = 2500$ kg/m^3 is the dust particle density, $g = 3.72$ m/s^2 is the gravitational acceleration, dp is the pressure gradient between vertical model layers, and $Q_{ext,\lambda}$ refers to the dust extinction efficiency at the particular wavelength under consideration.

Applying a column integration to the $d\tau_{d,si}$ in Equation 3 field returns

$$\hat{\tau}_{d,si} = \int_{column} d\tau_{d,si} \tag{4}$$

where $\hat{\tau}_{d,si}$ is the column integral of dust opacity. Up to this point, the dust distribution is self-consistently determined by the modeled circulation and parameterized dust processes. However, we now scale this opacity using the column dust climatology observations of Montabone et al. (2015); Montabone et al. (2020) (which is based on TES (Christensen et al., 2001), Thermal Emission Imaging System (THEMIS) (Christensen et al., 2004), and MCS (McCleese et al., 2007) observations available between MY 24 and MY 34), to find a scaling ratio as follows

$$\alpha_{scale} = \frac{\hat{\tau}_{d,obs}}{\hat{\tau}_{d,si}} \tag{5}$$

This is used to scale the dust opacity field in each radiative transfer time-step, which is $\Delta t_{ra} = 15$ min for the present GCM simulations. As the reference observations of Montabone et al. (2015); and Montabone et al. (2020) are two-dimensional maps of the daily column-integrated dust opacity, rescaling to the observations at a given instant within the day is determined by the linear interpolation between two successive days. It results in the scaled semi-interactive dust opacity field

$$\tilde{\tau}_{d,si} = \alpha_{scale} d\tau_{d,si} \tag{6}$$

which is then used by the model radiative transfer scheme. Here, the dust transport model we use is coupled to the correlated k-distribution radiation scheme of Mischna et al. (2012). The size-dependent extinction efficiencies, $Q_{ext,\lambda}$ as well as radiative scattering properties needed for radiatively active transport of dust particles, are treated by the two-moment framework of Lee et al. (2018).

In addition to the rescaling of the dust opacity field in Equation 6, we guide two transported tracers, q and N, using the computed scaling ratio α_{scale} (Equation 5), in each radiative transfer time-step as follows

$$
\begin{aligned}
\tilde{q}_{si} &= \alpha_{scale}\, q \\
\tilde{N}_{si} &= \alpha_{scale}\, N
\end{aligned}
\tag{7}
$$

where $\tilde{q}_{si}$ and $\tilde{N}_{si}$ are the scaled semi-interactive tracers, then being used by the radiative transfer scheme. This final step, that is, scaling of q and N, is quite essential to be able to consistently reproduce the dust storm onset and occurrence.

Lastly, it is worth adding that the process of dust lifting, by either dust devils or near-surface winds, follows the method of Newman and Richardson (2015).

3. Verification of the Dust Transport Model

The proper modeling of the dust cycle is of particular importance in terms of having more realistic CBL-dust interaction, especially within the lower atmosphere. Thus, the validity of the presented dust transport scheme is investigated, comparing the current GCM simulations to the MCS observations from Forget and Montabone (2017) and Kleinböhl et al. (2009) (from 12:00 h-16:00 h local time). To this end, Figures 1a and 1b display the vertical evolution of daytime dust mixing ratio at Oxia Planum (i.e., the landing site for ExoMars 2022) ($335.45°E, 24.55°N$) from our GCM simulations against the MCS retrievals, during the northern late winter ($L_s \sim 320°$) in Mars years 31 and 32.

In both simulated Martian years, our MarsWRF GCM simulations match well with MCS observations of dust mixing ratio from the CBL (below ~10 km in altitude) to the upper atmosphere (~60 km). Within the convective boundary layer in MY 31 and MY 32, the predicted dust mixing ratios in the GCM are consistent with those retrieved from MCS observations. In addition, the GCM simulations of MY 31 and MY 32 reproduce a high altitude tropical dust maximum (Heavens et al., 2011a; McCleese et al., 2010), which originates at ~30 km. Moreover, in Figures 1c–1f, we compare our GCM results with the available MCS observations (Heavens et al., 2011b) at different locations and seasons, such as in the north of Valles Marineris (MY29, $L_s \sim 163°$), southwest of Amazonis Planitia (MY29, $L_s \sim 165°$), west of Huygens Crater (MY29, $L_s \sim 166°$), and southwest of Gusev Crater (MY30, $L_s \sim 90°$). For these additional profiles, vertical variation of simulated dust opacity values are consistent with the MCS retrievals.

Figure 2 shows the seasonal variation of density-scaled dust opacity, calculated as follows:

$$
\overline{\tau}_d = log_{10}\, dz\tau_d/\rho \ [m^2/kg]
\tag{8}
$$

where τ_d is the dust opacity, ρ is the atmospheric density, and dz refers to the vertical thickness of the atmospheric layer (McCleese et al., 2010).

The latitude-height cross-sections are computed locally at 15h (LMST) for two longitudes: 25°W (passing through Oxia Planum) and 137°E (along Gale crater and Elysium Planitia, landing sites of MSL rover and InSight lander). For both longitudes, dust distribution contours confirm the enhancement in dust content during the dust storm season ($L_s \sim 225°$) compared to the northern spring ($L_s \sim 30°$) and summer seasons ($L_s \sim 135°$). To illustrate, the dust height maximum is at nearly 25 Pa (~32 km) before the dust storm season; however, it grows to as deep as 6 Pa (~47 km) due to the regional dust storms after $L_s \sim 180°$. The seasonal evolution of dust-top height is consistent with MCS retrievals of the dayside density-scaled dust opacity (see their Figure 11 in McCleese et al., 2010).

Furthermore, not only the dust-top altitude, but also the dust loading increases around $L_s \sim 225°$, where the dust cycle reaches nearly its peak activity as can be seen in column dust climatology observations (Montabone et al., 2015). Our GCM results during this period exhibit a sudden drop in dust content in the vicinity of 50°N. This structure, which can be interpreted as an abrupt dust content deficit, is also present at the same location in the Mars Climate Sounder (MCS) observations of McCleese et al. (2010).
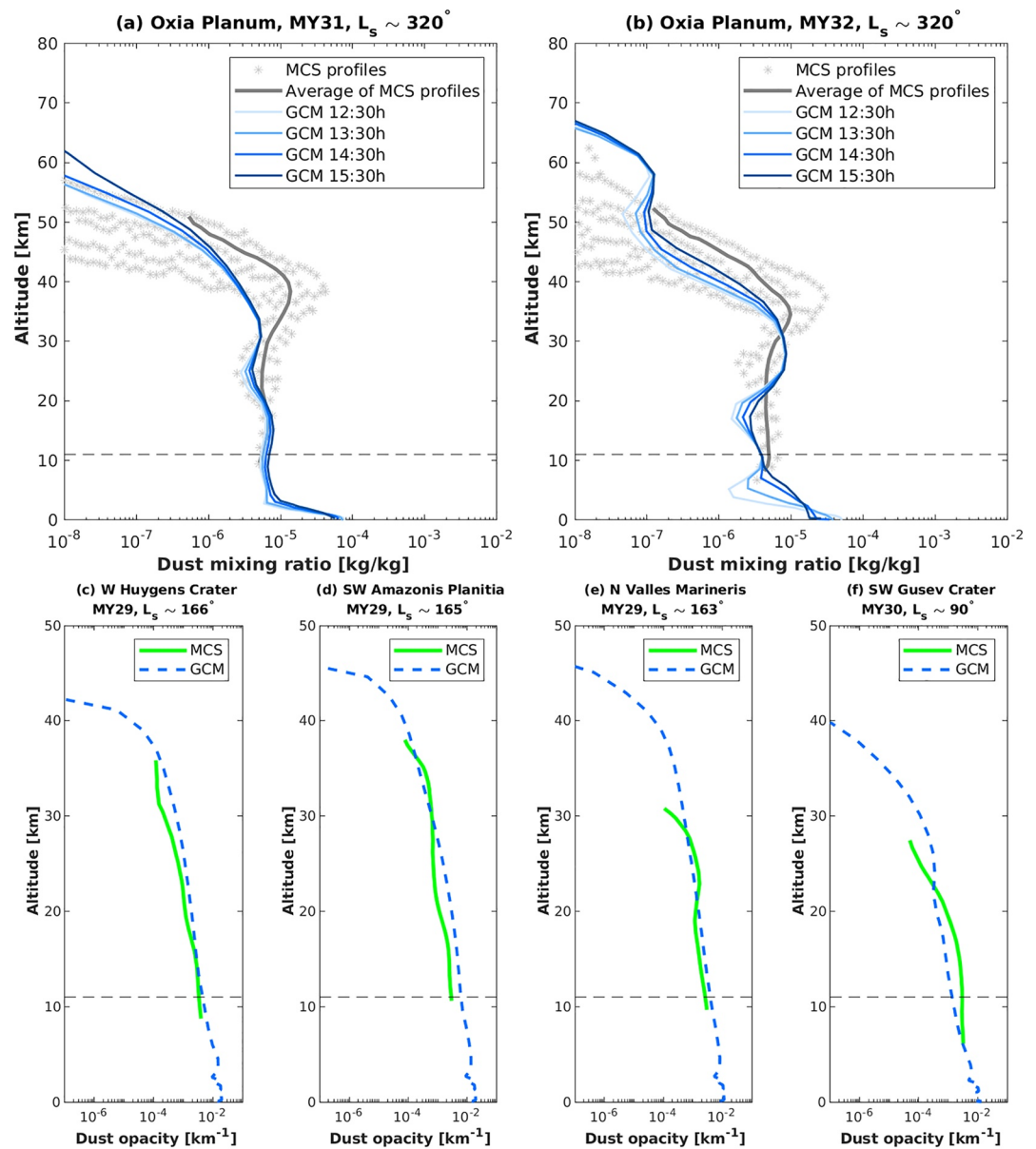
Figure 1. Vertical profiles of dust mixing ratio $[kg/kg]$ at Oxia Planum $(335.45°E, 24.55°N)$ in the northern late winter for Mars years (a) 31 and (b) 32. Colored solid lines indicate results from general circulation model (GCM) simulations at local afternoon, from 12:30 h to 15:30 h. Gray markers refer to the Mars Climate Sounder (MCS) observations reported in Forget and Montabone (2017) (between 12:00 h and 16:00 h), while the gray solid lines correspond to the average of retrievals having relative uncertainties in the dust opacity lower than 1 (see the details in Forget & Montabone, 2017). Vertical profiles of daytime dust opacity $[km^{-1}]$ from GCM (blue dashed lines) and MCS observations (Heavens et al., 2011b) (green solid lines) at the following locations and seasons: (c) West of Huygens Crater (MY29, $L_s \sim 166°$), (d) Southwest of Amazonis Planitia (MY29, $L_s \sim 165°$), (e) North of Valles Marineris (MY29, $L_s \sim 163°$), and (f) Southwest of Gusev Crater (MY30, $L_s \sim 90°$). The horizontal dashed line in each panel is the reference scale-height of Mars, that is, 11 km.

In Figure 3, we compare the seasonal evolution of dust effective particle radius retrieved from our GCM simulations, with respect to rover measurements at Gale crater. The measurements are obtained during the dust storm season of MY 31 and over a complete period of MY 32 using the UV sensor (UVS) of the Rover Environmental Monitoring Station (REMS) and the Mastcam instrument (Vicente-Retortillo et al., 2017). Results show that our GCM estimates exhibit a clear seasonal pattern matching well with the rover measurements in which both GCM and measurements decrease from 1.4 μm in northern early spring to 0.9 μm

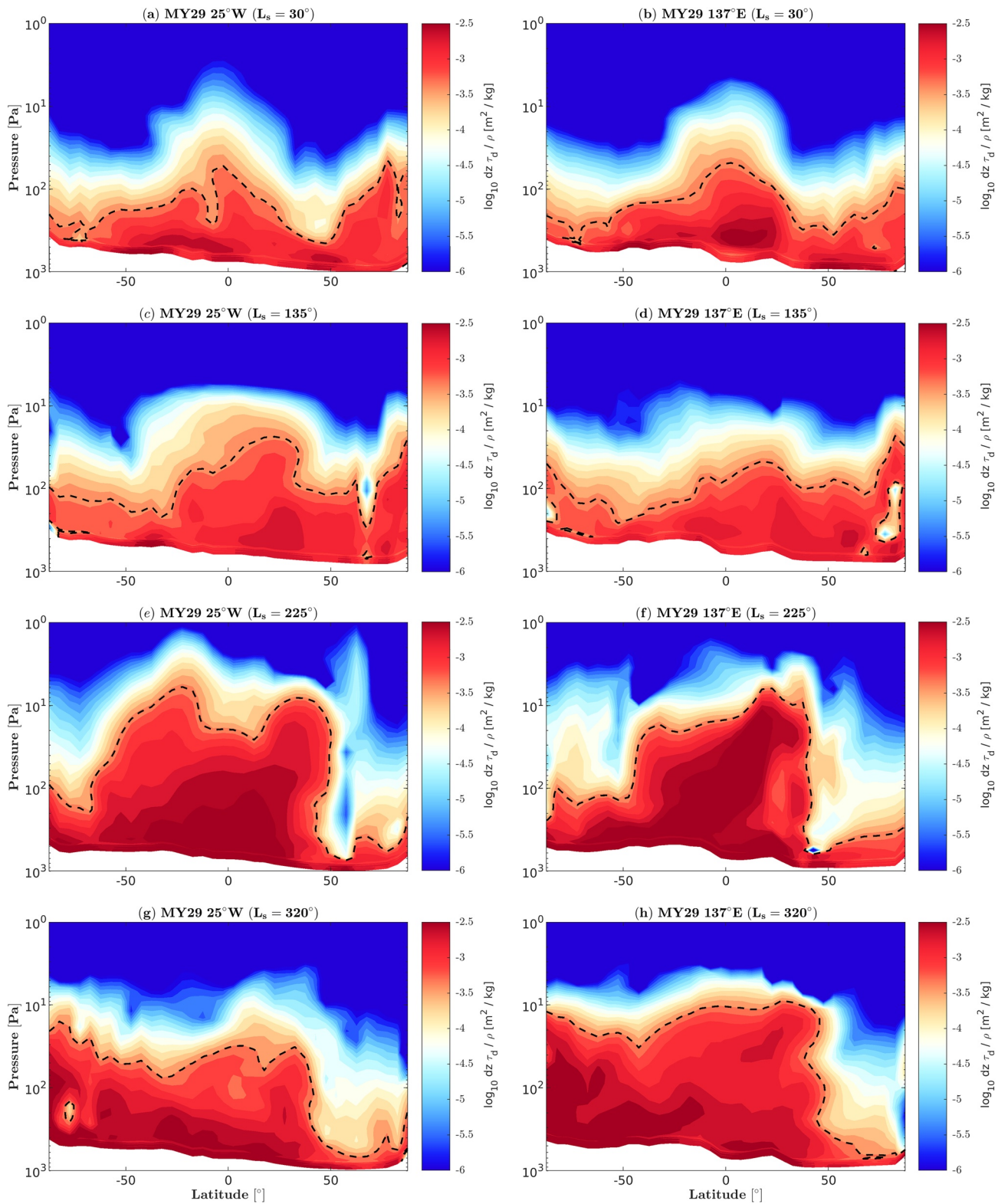**Figure 2.** Seasonal variation of density-scaled dust opacity, $log_{10}\ dz\tau_d/\rho\ [m^2/kg]$ in MY 29 at $t = 15h$ (LMST). Latitudinal and vertical cross-sections are plotted at two longitudinal locations over $25°W$ (left panels) and $137°E$ (right panels). Black dashed lines represent the dust-top height, calculated at the altitude where the $\overline{\tau}_d = -3.3$, following Wu et al. (2020).
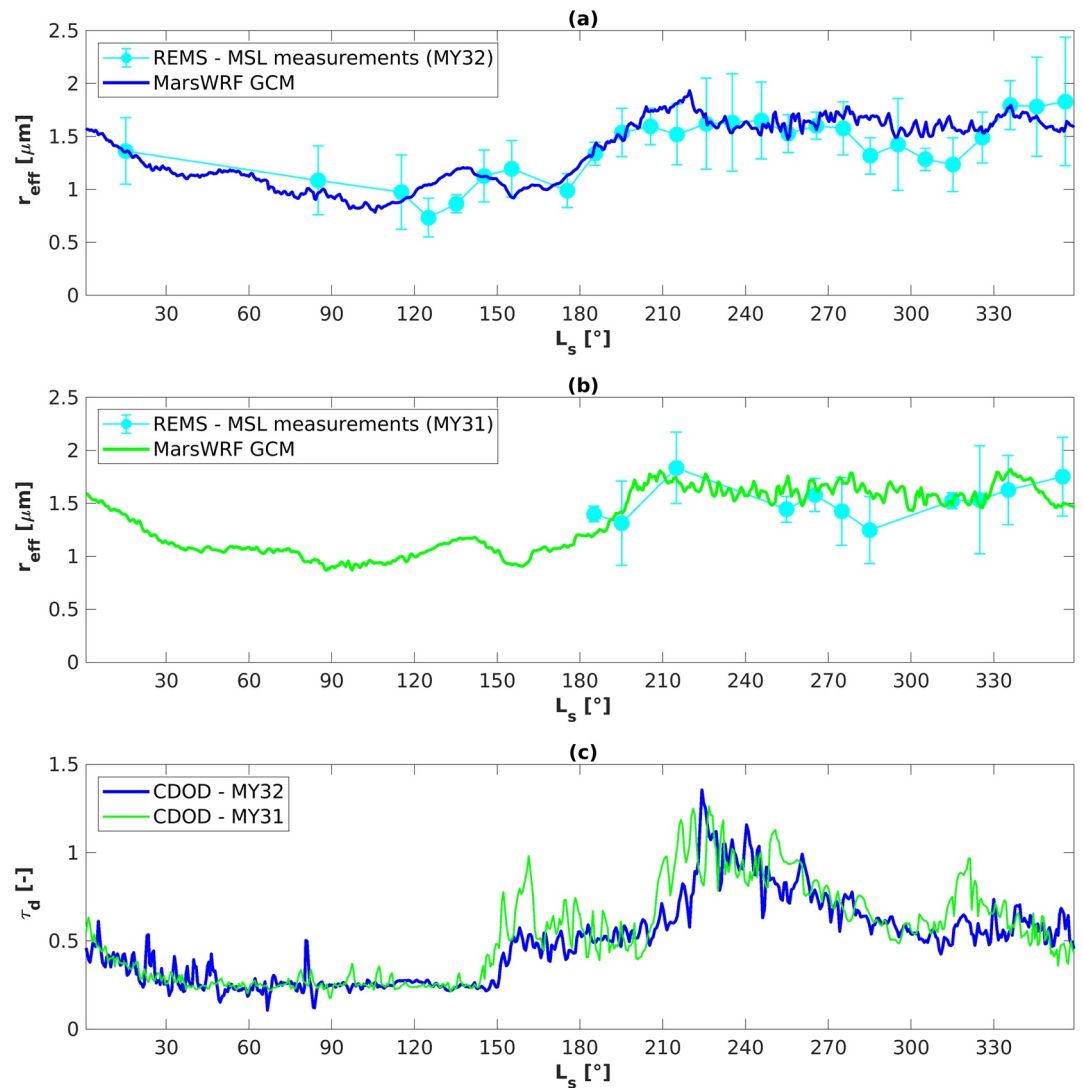
Figure 3. Seasonal evolution of dust particle effective radius through MY 32 (a) and MY 31 (b) above Gale crater. Blue (MY 32) and green (MY 31) solid lines show our general circulation model (GCM) simulations with semi-interactive dust transport model. Light-blue solid lines with error bars refer to the rover measurements using the UV sensor (UVS) of the Rover Environmental Monitoring Station (REMS) and the Mastcam instrument, from Vicente-Retortillo et al. (2017). (c) Seasonal variation of column dust optical depth (CDOD) referenced to 700 Pa based on the dust climatology observations of Montabone et al. (2015) in MY 31 and MY 32.

in northern summer when the column-integrated dust opacity is as low as $\tau_d = 0.3$ (before the dust storm season). However, dust r_{eff} values are considerably enlarged with the growing dust activity in dust storm season where the column-integrated dust opacity exceeds ∼1.

4. GCM Results

4.1. Seasonal and Interannual Variations

Thanks to observations by recent in-situ and orbiter missions, current knowledge of the Martian convective boundary layer has been progressing in terms of observing day-side characteristics for particular locations. Nevertheless, long-term variations (i.e., seasonal and year-to-year) on a more global scale are less well constrained. To probe the long-term behavior of Martian boundary layer activity, we assess a decade-long GCM simulation from MY 24 through MY 34, using our Mars-specific PBL scheme (Temel et al., 2020) and the present semi-interactive dust transport model. Note that we use a 5° x 5° spatial grid resolution with 52

vertical sigma layers extending up to a model top of ~100 km. As this decade has three GDS in MY 25, MY 28, and MY 34, particular attention is given to the impact of GDS on the planetary boundary layer. We first investigate the seasonal and interannual trends in convective boundary layer activity by discussing two recent Martian years, MY 33 and MY 34. Given the fact that the global dust storms are an important perturbing force in the present Martian climate, the chosen years, MY 33 (without a GDS) and MY 34 (with a GDS), allow us to deduce the extent of the CBL response to the GDS. Therefore, in Figure 4, the annual variation of CBL diagnostics is illustrated for MY 33 over the full span of latitudes. In Figure 4a, the zonal averaged CBL depth evolution is displayed through MY 33, which is one of the key parameters characterizing CBL dynamics. Here, the depth of CBL refers to the altitude that marks the transition from a highly turbulent convective atmosphere below to the nonturbulent, stable, free-atmosphere above. In other words, the depth of the CBL marks the upper boundary of a highly turbulent region, being well mixed by means of highly energetic eddies and deep convective plumes. We determine the top of CBL in the GCM, through our PBL scheme implementation (Temel et al., 2020), as the first vertical sigma level where the local potential temperature, θ_σ, surpasses the potential temperature of the mixed layer, θ_m, by a threshold of $\Delta\theta_t = 0.5$ K. The given approach is referred to as the θ-increase method, derived from terrestrial assessments (Heffter, 1980; Hu et al., 2010; Nielsen-Gammon et al., 2008). Note that the mixed layer here corresponds to the major portion of CBL, that is, from about 10% to 85% of the CBL depth, where the turbulence leads to a well-mixed exchange of momentum, heat, and aerosols (Hinson et al., 2019; Stull, 2012; Senel et al., 2020). The mixed layer lies over the atmospheric surface layer (i.e., the lowermost portion of the CBL and up to 10% of CBL depth), with an almost uniform θ that is nearly equivalent to the base potential temperature of the surface layer. Note that the atmospheric surface layer refers to the lowermost portion of the CBL, extending from the surface up to the Monin-Obukhov length, which is typically of the order of tens of meters (Davy et al., 2010; Martínez et al., 2009). Separate from the θ-increase method, the depth of the CBL is calculated in the RO experiments based upon the vertical gradient of potential temperature, that is, the static stability method. This approach treats the CBL depth as the first model layer when the local vertical gradient of potential temperature reaches a threshold lapse rate of 1.5 K/km. Figure 4a, more specifically, shows the CBL depth evolution for the local afternoon at $t = 15$ h, when the convective boundary layer activity can nearly reach its peak activity (Martínez et al., 2009; Spiga et al., 2010). Note that the results here are displayed in terms of zonally averaged values (i.e., averaging the values in the longitudinal direction at a fixed local time, $t = 15$ h), to see the CBL depth variabilities through the meridional direction over different seasons. For detailed spatial variations toward both zonal and meridional directions in CBL characteristics, see Section 4.2. In Figure 4a, the peak CBL depth has a seasonal pattern that is roughly symmetric about the equator, propagating to the northern tropics (~20–30°N) during northern summer and then back to the southern tropics (~20–30°S) during the northern winter. This seasonal variation results in two seasonal maxima in CBL depth of up to ~9 km, which correspond to the peak convective heating of the surface during local summer. The latitudinal variation of the peak CBL depth as a function of season coincides nearly with the location of Hadley cell convection, shifting up and down toward the tropics during northern summer and winter seasons (i.e., in line with the surface temperature evolution in Figure 4d). As the convective boundary layer deepens further, which is enhanced by the abundance of turbulent convection (see Section 1), these two maxima represent the extremity of production rate in terms of turbulent convection, where the boundary layer rises to in excess of 9 km in depth.

To clarify this better, the annual variation of surface kinematic heat flux, q_s is presented in Figure 4c and Deardorff's convective velocity scale (also known as the convective velocity), w_*, is shown in Figure 4e. The first parameter, $q_s = \mathcal{H}_s / (\rho_a C_p)$, is the measure of convecting heat flux from the surface, defined as the surface sensible heat flux, $\mathcal{H}_s$, normalized by the specific heat capacity, $C_p = 740 \ JK^{-1}kg^{-1}$, and the surface air density, ρ_a, (Petrosyan et al., 2011). The second parameter, $w_* = [(g/T_s)q_s z_i)]^{1/3}$, is Deardorff's velocity scale, which represents the speed of turbulent convection (Deardorff, 1970), where $g = 3.72$ m/s^2 is the average gravitational acceleration on Mars, T_s is the surface temperature, and z_i is the CBL depth. Remembering that the planetary boundary layer is exposed to growing surface solar heating especially around the local noon (Newman, Kahanpää, et al., 2019; Ordonez-Etxeberria et al., 2018), this tends to intensify the surface heat flux of rising convective plumes, q_s, which moves upward faster as given by the convective velocity, w_*. Therefore, the depth of the CBL, z_i, is positively correlated with the enhancement in q_s and w_*. In other words, the lower (higher) the q_s and w_* are, the shallower (deeper) the planetary boundary layer

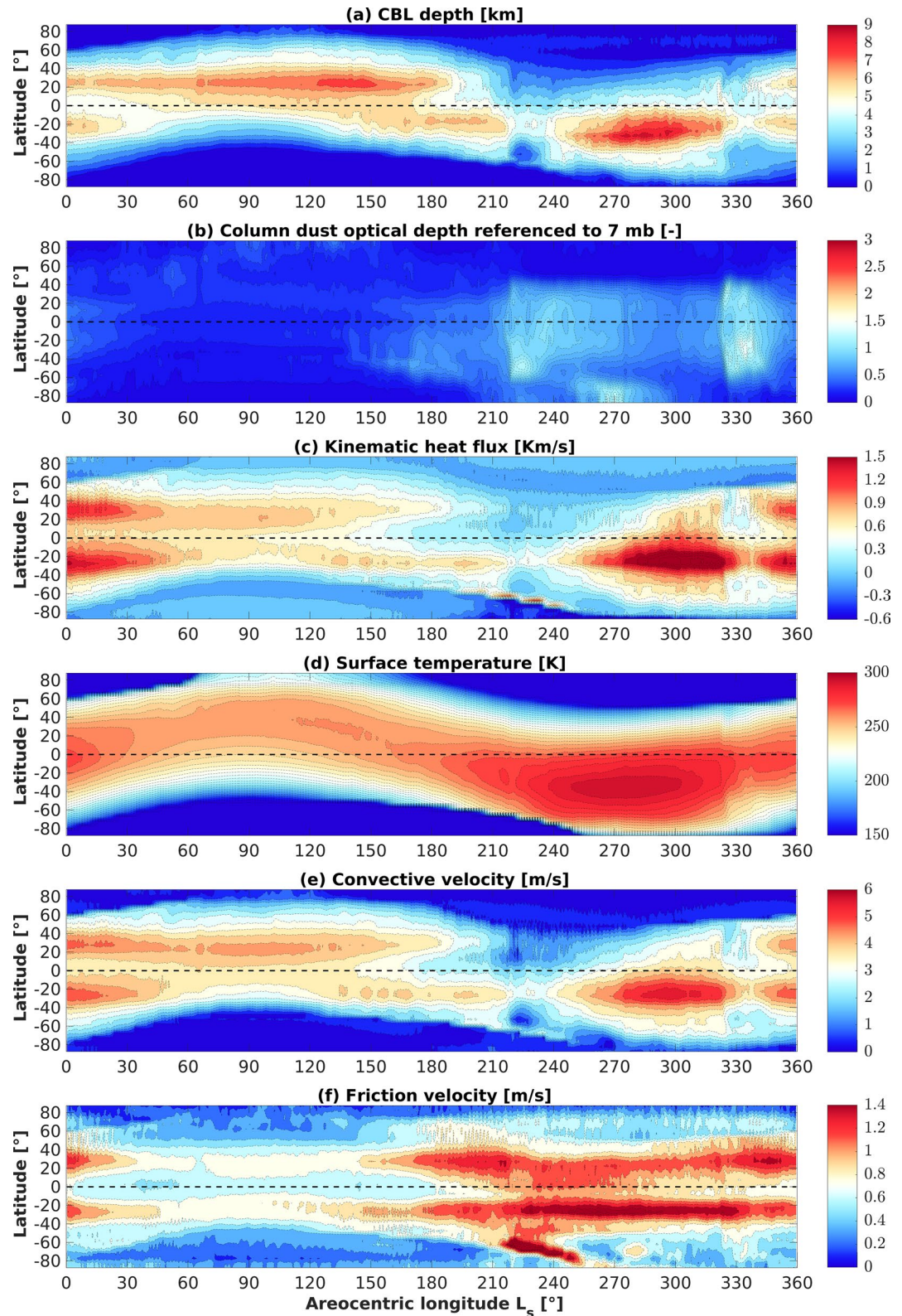**Figure 4.** Annual variation of the zonally averaged (a) convective boundary layer (CBL) depth, (b) column dust optical depth referenced to 7 mb, (c) surface kinematic heat flux, (d) surface temperature, (e) Deardorff's convective velocity, and (f) friction velocity. Here, the simulated case is Mars Year 33 in the local afternoon, $t = 15h$ (LMST). Note that the color bar limits are set to the same range as in Figure 5.

is. In Figure 4a, the CBL depth during MY 33 is as shallow as a few kilometers at higher latitudes and in the vicinity of the polar caps. Yet, it is as deep as ~9 km around the tropics, even exceeding 9 km in depth around the northern midsummer. This broad range is consistent with the radio occultation measurements of Hinson et al. (2008); and Hinson et al. (2019) in which the daytime CBL depth ranges between 1 and 10 km. In these measurements, the depth of CBL ranges from a few kilometers in high latitudes (i.e., z_i = 1.5 km) up to depths as deep as z_i ~9–10 km through the tropics. This significant change is largely driven by the interrelation of turbulent convection and shear forcing, as explained below. Given the seasonal evolution of turbulent convection in Figures 4c–4e, it likely confirms the positive correlations of q_s and w_* with the CBL depth. However, the periods of northern early spring (L_s ~ 0–30°) and from the northern late summer to the early autumn (L_s ~ 150–210°) are an exception, due to the negative feedback of high shear production on the growth of convective boundary layer. The latter is given in terms of friction velocity, u_* (Figure 4f), indicating high friction velocities in these two particular periods, that is, compared to the typical mean daytime value of the Martian CBL, being ~0.4 m/s (Petrosyan et al., 2011). Note that the influence of shear production on the CBL will be discussed in greater detail below. In addition, the convective velocity field in Figure 4e ranges from nearly 3 m/s to 6 m/s, corresponding to the regions where a shallow and deep CBL form, respectively. This range in w_* from our GCM simulations agrees well with the turbulence-resolving large-eddy simulations of Spiga et al. (2010), where w_* ~3–6 m/s around t = 15h (LMST), also with values obtained using ground-based observations in combination with the similarity theory by (Martínez et al., 2009). Note that the value of w_* is nearly 1 − 2 m/s for a typical CBL on Earth (Kaimal et al., 1976; Moeng & Sullivan, 1994). Furthermore, as with the seasonal variation of w_*, Spiga et al. (2010) retrieve a surface kinematic heat flux as high as q_s = 2 Km/s around t = 15h (LMST), as is the case in our GCM simulations presented in Figure 4c. Regarding the deepest CBL formation (i.e., above 7 km), there exists two seasonal maxima. The first maximum evolves continuously between L_s ~ 125 and 150° over the northern tropics (~20–30°N). It is associated with a higher rate of turbulent convection (Figure 4e) and surface temperature (Figure 4d) augmented by radiative heating (Figure 4c) during the northern summer season. Later, the second maximum forms, extending from the northern late autumn toward the northern early winter (i.e., L_s ~ 255–310°). A sudden drop in CBL depth over southern tropics takes place between L_s ~ 210 and 240°, which marks the occurrence of regional dust storm activity, as is observed in the annual evolution of column dust optical depth (CDOD) referenced to 700 Pa (Figure 4b). As MY 33 did not experience a GDS event, it can be considered a quiescent year in terms of dust abundance. However, two particular periods within the dust season (the northern late autumn and late winter, respectively) perturb the convective boundary layer through regional dust storms, during which the normalized CDOD of the planet reaches nearly 1. The presence of increased dust loading reduces surface-to-atmosphere temperature contrasts, producing a more stable lower atmosphere that weakens the convective activity, lowering the CBL depth by ~2 km.

Despite the high rates of surface heating and temperature over the southern tropics (Figures 4c and 4d) from late spring until early summer (L_s ~ 240–320°), this does not ensure further enhancement in CBL activity of extremely deep layers exceeding 9 km. To illustrate, Figure 4a indicates that the second CBL maximum (occurring between L_s ~ 255–310°) exhibits similar CBL depths compared to the first CBL maximum (in the northern summer L_s ~ 125–150°). This is due to the high rates of shear forcing in the southern tropics (Figure 4e), amplified by the regional dust storm of MY 33 commencing at L_s ~ 210° (Figure 4b). Figure 4f demonstrates the friction velocity, u_*, which is the velocity scale of surface shear forcing. In other words, the friction velocity, $u_* = (\tau_s/\rho_a)^{1/2}$, denotes the surface shear flux, τ_s, which is normalized by the air density, ρ_a. Growing friction velocity implies higher shear production, originating from the shear instabilities, which can be augmented by local dust events or the Hadley circulation strength. That, in turn, inhibits the convection and caps the growth of the CBL. Such a type of boundary layer is called shear-dominated CBL, unlike the purely buoyant CBL. To illustrate the difference on Earth (Moeng & Sullivan, 1994), a typical purely buoyant CBL doubles in depth (z_i ~1 km), with respect to a shear-dominated CBL (z_i ~0.5 km) through the shear/buoyancy interaction. This could explain why the second CBL maximum during the northern winter (Figure 4a) is not capable of growing further in depth, as it is capped by the dust-induced shear instabilities. Unlike the relatively quiescent MY 33, MY 34 exhibits extreme dust activity (Kass et al., 2020). As illustrated in Figure 5b, MY 34 has one large/massive peak in dust opacity, northern autumn starting shortly after northern autumn equinox, corresponding to the planet-encircling GDS, which is followed by a smaller peak during northern late winter, corresponding to a large regional storm. Here, as can be seen, the
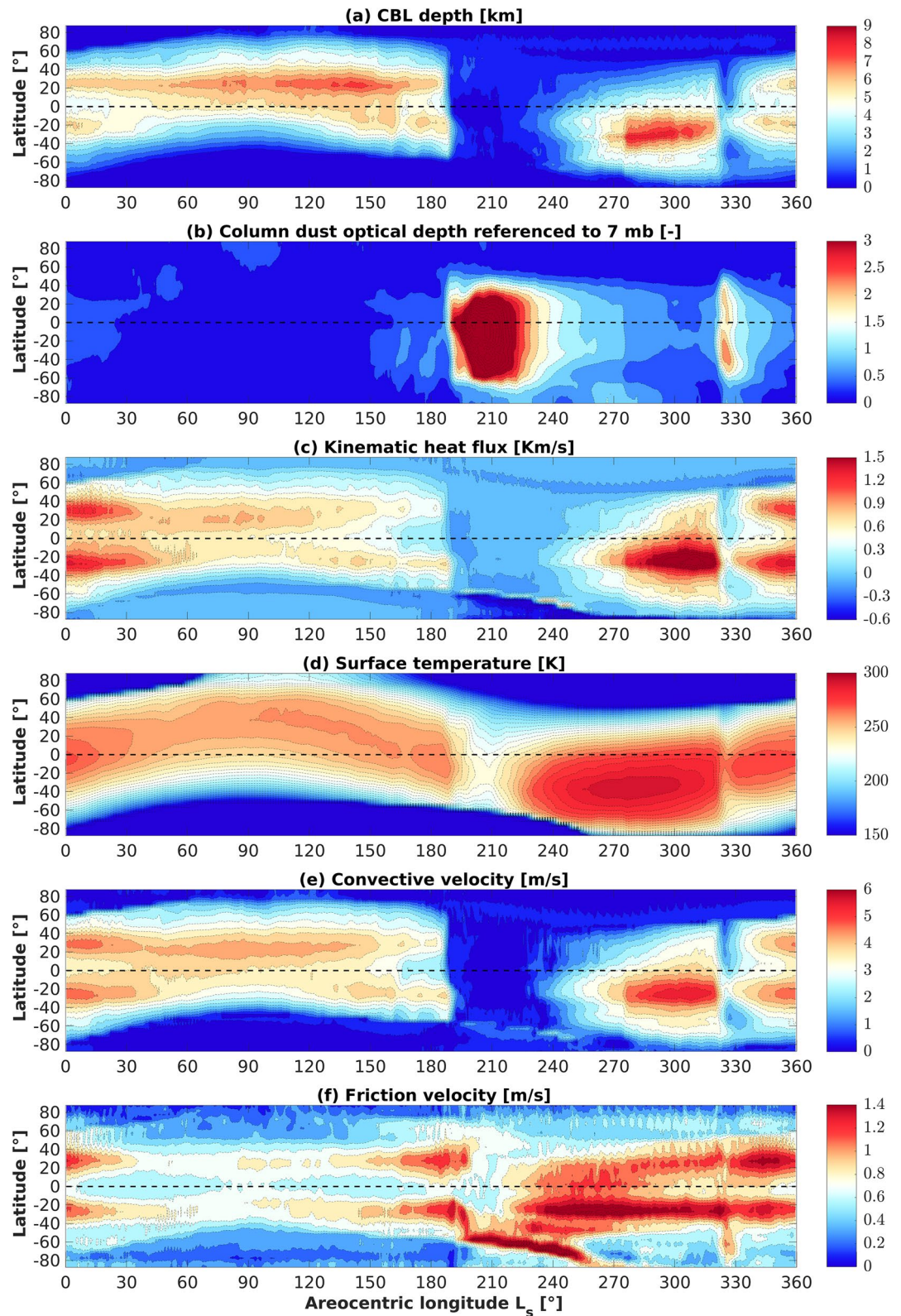
Figure 5. As in Figure 4 but now showing results for Mars Year 34.

present semi-interactive dust transport model performs adequately to capture the onset and occurrence of dust storms (being either a global or regional dust storm event). More specifically, the first peak shows the trace of an extreme dust event engulfing almost the whole planet for a long period. The global dust storm of MY 34, hereafter GDS-34, lasts more than 100 sols between $L_s \sim 185$ and 250°. Moreover, its intensity rises to in excess of three in terms of CDOD referenced to 700 Pa, covering most of the planet from the southern high latitudes to northern midlatitudes. As the dust particles block the incoming sunlight, such a long-term residency of a much higher dust abundance implies a severe consequence in terms of radiative heating inhibition. Accordingly, a strong internal cooling occurs within the CBL and a drastic reduction of radiative heating (Figure 5c) and surface temperature (Figure 5d) during $L_s \sim 185$–250°.

The effect of global dust storms can also be seen in Figures 6a and 6b, showing the interannual variability of globally averaged surface kinematic heat flux and temperature throughout the last decade on Mars. Results indicate that the surface daytime radiative flux is exposed to long-lasting attenuation while massive dust storms hit the planet, even in the afternoon, despite the peak rate of convective activity. Our GCM results show that surface level daytime solar fluxes are strongly attenuated during the larger dust storms, offsetting the increased convective activity for all the GDS events recorded during MY 25, MY 28, and MY 34. Nevertheless, only the events of GDS-25 and GDS-34 were able to drastically diminish thermal convection, reversing the thermal process as a prolonged surface cooling. Results show that the global average daytime surface kinematic heat flux, q_s, drops from ~0.35 Km/s (at the onset of the storm) to below 0 Km/s by the time the mature phase is reached (at $L_s \sim 210°$). The period of surface cooling lasts for at least 95 sols (i.e., $L_s \sim 189$–249°) during GDS-25 and for nearly 82 sols (i.e., $L_s \sim 191$–242°) during the most recent global dust event on Mars, that is, GDS-34 (Figure 6a). Related to the extreme surface cooling, the global average surface temperature (Figure 6b) drops by nearly 22 K in GDS-25 and nearly 20 K in GDS-34. As a consequence of higher cooling rates within the boundary layer, the production rate of turbulent convection is drastically diminished during GDS-25 and GDS-34, relative to the quiescent years. For instance, in Figure 6c, the velocity scale of turbulent convection, w_*, is depicted in terms of an equatorial time series for each simulated Martian year. For both GDS-25 and GDS-34, the global average of w_* drops from ~3 m/s at the onset of the storm to as low as ~0.5 m/s during the mature phase of the storm. Similarly, w_* drops from ~3.5 m/s to ~1.5 m/s between the onset and mature phase of the GDS-28 storm, which occurs later in the year. Besides the key effect of a GDS on the boundary layer, that is, blocking the surface radiative heating, thus, a global weakening in convective activity, a secondary effect is the shear forcing alteration, in which a minor weakening of friction velocity occurs during the onset of GDS-34 ($L_s \sim 180$–210°) and restrengthening afterward ($L_s \sim 210$–270°), as shown in Figure 5f. Moreover, for the friction velocity, we report strong seasonal variations, as high as 50% during the dust storm season (after $L_s \sim 180°$), by inducing enhanced shear instabilities within the boundary layer. To illustrate, the equatorial friction velocity grows from ~0.75 m/s (prior to storm onset) up to ~1.1–1.2 m/s within the dust storm season for each simulated Martian year (Figure 6d). So far, we have outlined the key and secondary effects of a GDS, acting negatively on the turbulent convection. Due to extreme dust abundance and the ensuing highly turbulent surface winds, a global dust storm massively inhibits convective activity. To deduce its effect on the convective boundary layer, we examine the annual evolution of CBL depth through MY 33 and MY 34, retrieved from the GCM results in Figures 4a and 5a. Unlike the quiescent MY 33, a large amount of dust was injected into the atmosphere during GDS-34 (Figure 5b), causing extremely shallow boundary layers. It becomes as shallow as a few hundred meters, covering the entire planet from the equator toward the polar caps (Figure 5a). This results in a planet-wide boundary layer with the same depth as an extremely shallow daytime boundary layer; hence, we describe it as a "global-darkness" state of the Martian CBL, persisting for nearly 100 sols, that is, $L_s \sim 185$–250°. The interannual variability in equatorial (Figure 6f) and zonally averaged (Figure 7) CBL depth is illustrated from MY 24 to MY 34. The main interannual variability occurs especially during global dust storms. To illustrate, while passing through GDS-34, the depth of the CBL experiences an excessive drop from 6 km down to as shallow as 0.5 km; the same is true for GDS-25. The impact of GDS-28 differs from that of GDS-25 and GDS-34 in a way such that GDS-28 could not globally negate surface kinematic heat flux (Figure 6a), since GDS-28 has nearly half the CDOD in terms of storm intensity (Figure 6e). Thus, GDS-28 still features a relatively higher convective boundary layer with a depth around 1.5–2 km, even at the most mature phase of the storm (Figure 6f). Therefore, in contrast to GDS-25 and GDS-34, GDS-28 could not form an extremely shallow daytime boundary layer near the equator. Even though extremely shallow daytime boundary layers
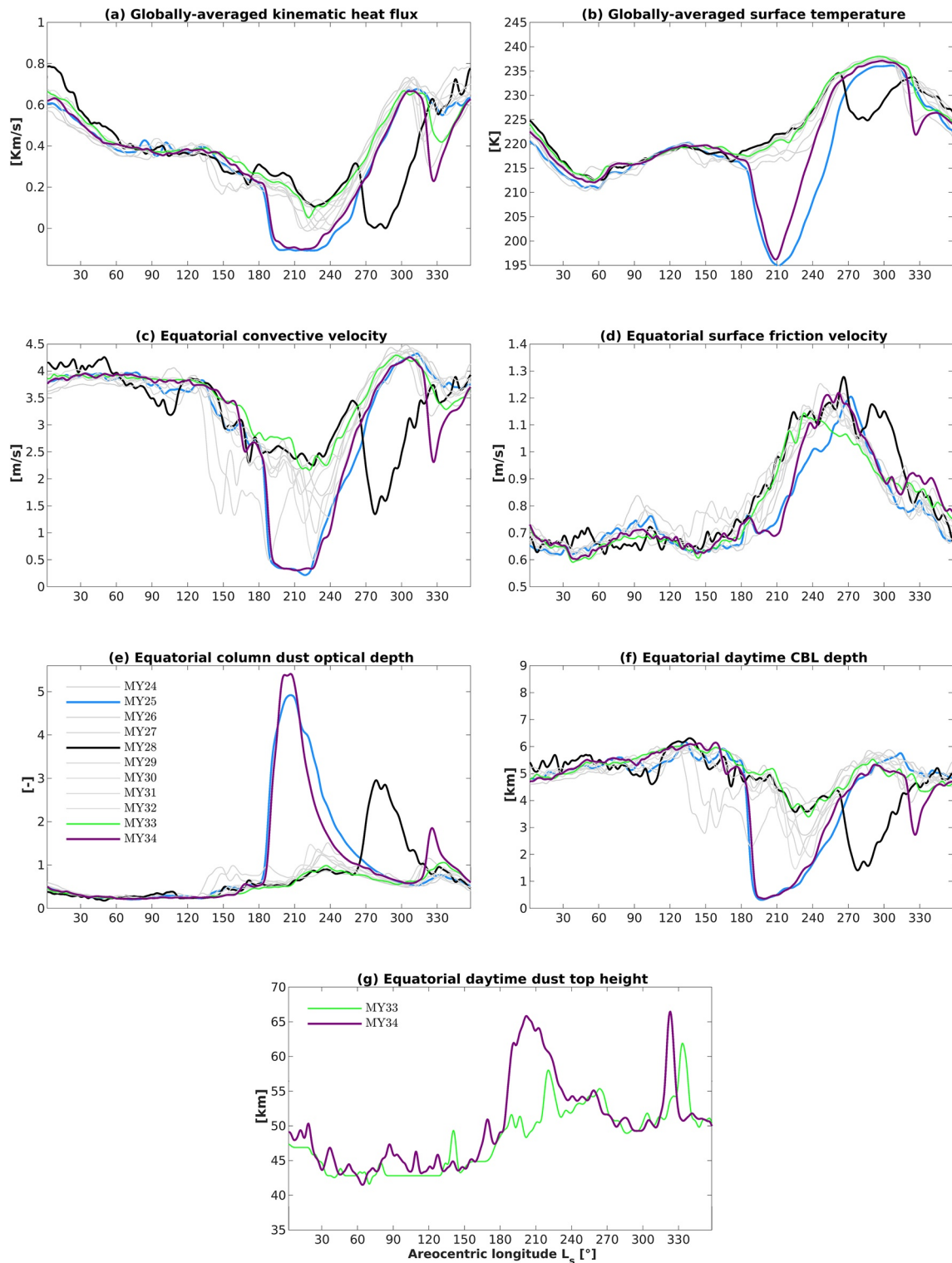
Figure 6. Interannual variation of simulated globally averaged (a) surface kinematic heat flux, (b) surface temperature; and equatorial (c) Deardorff's convective velocity, (d) friction velocity, (e) column dust optical depth (CDOD) referenced to 7 mb, (f) daytime CBL depth, and (g) daytime dust top height, shown for MY 24 through 34 in the local afternoon, $t = 15h$ (LMST).
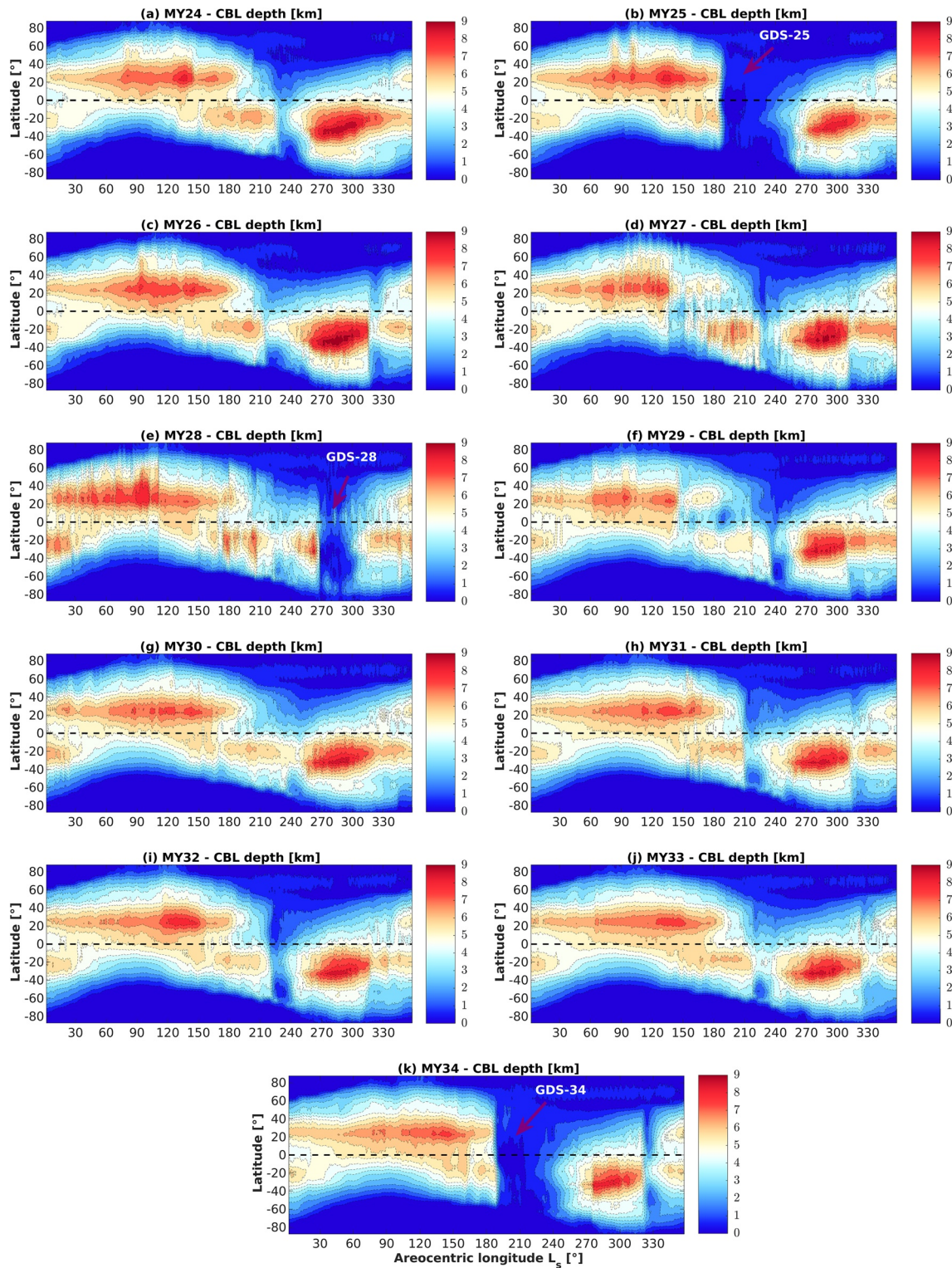
Figure 7. The decade-long evolution of zonally averaged convective boundary layer (CBL) depth from MY 24 to MY 34, in the local afternoon, $t = 15h$ (LMST). Global dust storms (GDS)-25, GDS-28, and GDS-34 are the global dust storm events occurring in MY 25, MY 28, and MY 34, respectively.

form especially over southern midlatitudes in GDS-28, they are not as long-lasting as in GDS-25 and GDS-34 events (Figure 7). Finally, we also examine the annual evolution of daytime dust-top altitude near the equator, determined as following Wu et al. (2020). This is shown in Figure 6g for Mars years 33 and 34. The daytime dust-top altitude remains nearly constant at z_{max} ~43 km before the dust storm season, without any significant interannual variability. Following the start of the dust storm season, however, the daytime dust top is substantially raised in line with the growing dust activity (which is properly reproduced by the new semi-interactive dust transport model). The daytime dust top height rises to ~57 km for the quiescent year (MY 33) when there is no global dust storm. Yet, it extends up to ~65 km during GDS-34.

4.2. Regional Variations

In addition to the seasonal and interannual variations presented above, Martian surface meteorology is also affected by the various complex features on its surface. To better understand CBL dynamics induced by regional effects, we show the variability of CBL depth, z_i, in northern (Figure 8a) and southern (Figure 8b) early summer seasons for MY 33, in the local afternoon, $t = 15h$ (LMST) at all locations. Besides, the velocity scales of turbulent convection, w_*, and shear forcing, u_*, in northern early summer are depicted in Figures 8c and 8d, respectively. First, the evolution of the polar caps is evident on the geographical variations of CBL depth (Figures 8a and 8b), by altering the turbulent convection (i.e., in terms of Deardorff's convective velocity, w_*, in Figure 8c). The polar ice caps are the result of the Martian CO_2 and water cycles, driven by the planet's orbital eccentricity and obliquity. For instance, during the northern winter season, water and CO_2 ice will be accumulated on the surface of the northern polar region. The accumulation of water as well as the increase in areal coverage of CO_2 will increase the surface albedo. Therefore, the more reflective surface will lead to negative surface kinematic heat fluxes (referring to the surface cooling) and a decrease in the level of turbulence within the planetary boundary layer. Consistently, very low CBL depths (up to only a few 100 m) are estimated in northern winter around the northern polar cap (Figure 8b) and in southern winter around the southern polar cap (Figure 8a) (see the zonally averaged CBL depths over polar caps in Figure 9). In other words, the Martian PBL poleward of 80°N-S is stably stratified, which is mostly observed during nighttime conditions (Petrosyan et al., 2011). Such a shallow formation of a stably stratified PBL, even during daytime conditions (Figures 8a and 8b), is associated with very low values of surface kinematic flux around the polar caps (see Figure 5c). In addition to high cooling rates, the polar caps show low friction velocities (u_* ~0.3 m/s) (Figure 8d). Given the fact that the stably stratified PBLs with weak near-surface winds, that is, the so-called very stable boundary layers (vSBL) are observed on Earth (Grachev et al., 2005), a similar type of PBL may occur in the northern polar region of Mars.

For midlatitude and equatorial regions in the northern midsummer season, the highest CBL depths, in excess of 9 km (Figure 8a), occur in the vicinity of Tharsis Montes, Olympus Mons, Alba Mons, and Elysium Mons (see the locations of these regions in Figure 8f). The higher the elevation, the lower the surface pressure and the surface atmospheric density. This implies that the turbulent mixing in the CBL will be deeper with the same amount of turbulent flux, for the case where the planetary boundary layer develops in lower-pressure regions, consistent with Spiga et al. (2010). This effect on the CBL can also be seen in such locations as the Hellas basin and Argyre Planitia (as in Figure 8b). Both regions are located below the MOLA reference elevation (D. E. Smith et al., 2001) and thus have higher surface pressures compared to other equatorial and midlatitude regions. Therefore, for these regions, CBL depth can be as low as 3–4 km, as shown in Figure 8b.

In addition to terrain elevation, surface thermal inertia also plays an important role in surface meteorological conditions and thus CBL dynamics on Mars. For the northern midsummer map of CBL depth in Figure 8a, similar to Tharsis Montes, we find that deep CBLs form in the Amazonis Planitia, Arabia Terra, Alba Patera, and Elysium Mons regions, which have lower thermal inertia compared to other midlatitude regions (see Figure 5 of Putzig et al., 2005 for the thermal inertia map of Mars). Thanks to their lower surface thermal inertia, temperature variations from night to day are greater in those regions. Thus, turbulent convection is enhanced and leads to a deeper CBL. Likewise, higher surface thermal inertia values mark relatively shallower CBL formation over the tropics, with a CBL depth of ~5 km, such as in the Elysium Planitia, Xanthe Terra, and Valles Marineris regions (Figure 8a). Another important effect of surface thermal
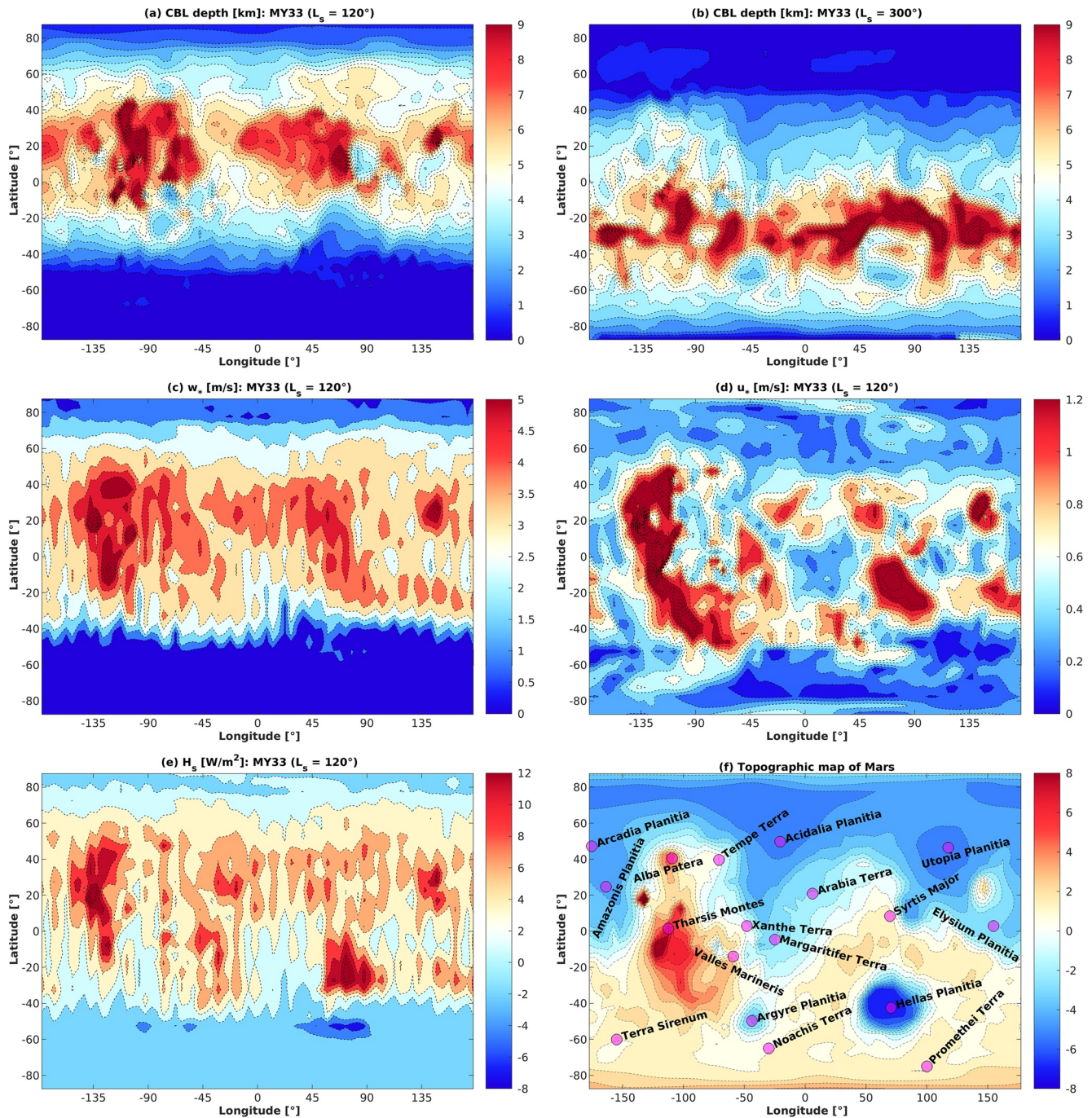
Figure 8. The regional variability in MY 33, in terms of the convective boundary layer (CBL) depth in the northern early summer ($L_s = 120°$) (a) and southern early summer ($L_s = 300°$) (b), in the local afternoon, $t = 15h$ (LMST) at all locations. Deardorff's convection velocity, w_*, (c), the friction velocity, u_*, (d) and surface sensible heat flux, $\mathcal{H}_s$, (e) are depicted in the northern early-summer season. Locations of some particular regions addressed in the present study, marked on the topographic map of Mars (f) based on Mars Orbiter Laser Altimeter (MOLA) data (D. E. Smith et al., 2001).

inertia is related to the near surface winds. Stanzel et al. (2006) reported that high near-surface winds can be observed in Amazonis Planitia. We show that the heterogeneous thermal surface forcings, as a result of the spatial gradients of the thermal inertia with respect to its neighboring regions, can amplify the near-surface winds (similarly to slope winds or cap-edge winds driven by horizontal contrasts in surface properties). It is worth noting that the presence of heterogeneous thermal surface forcings is noticeable in terms of surface sensible heat flux (Figure 8e), exhibiting a high zonal variation, which accordingly causes high zonal

Figure 9. The annual evolution of the zonally averaged daytime convective boundary layer (CBL) depth in the northern (left panels) and southern (right panels) hemispheres. The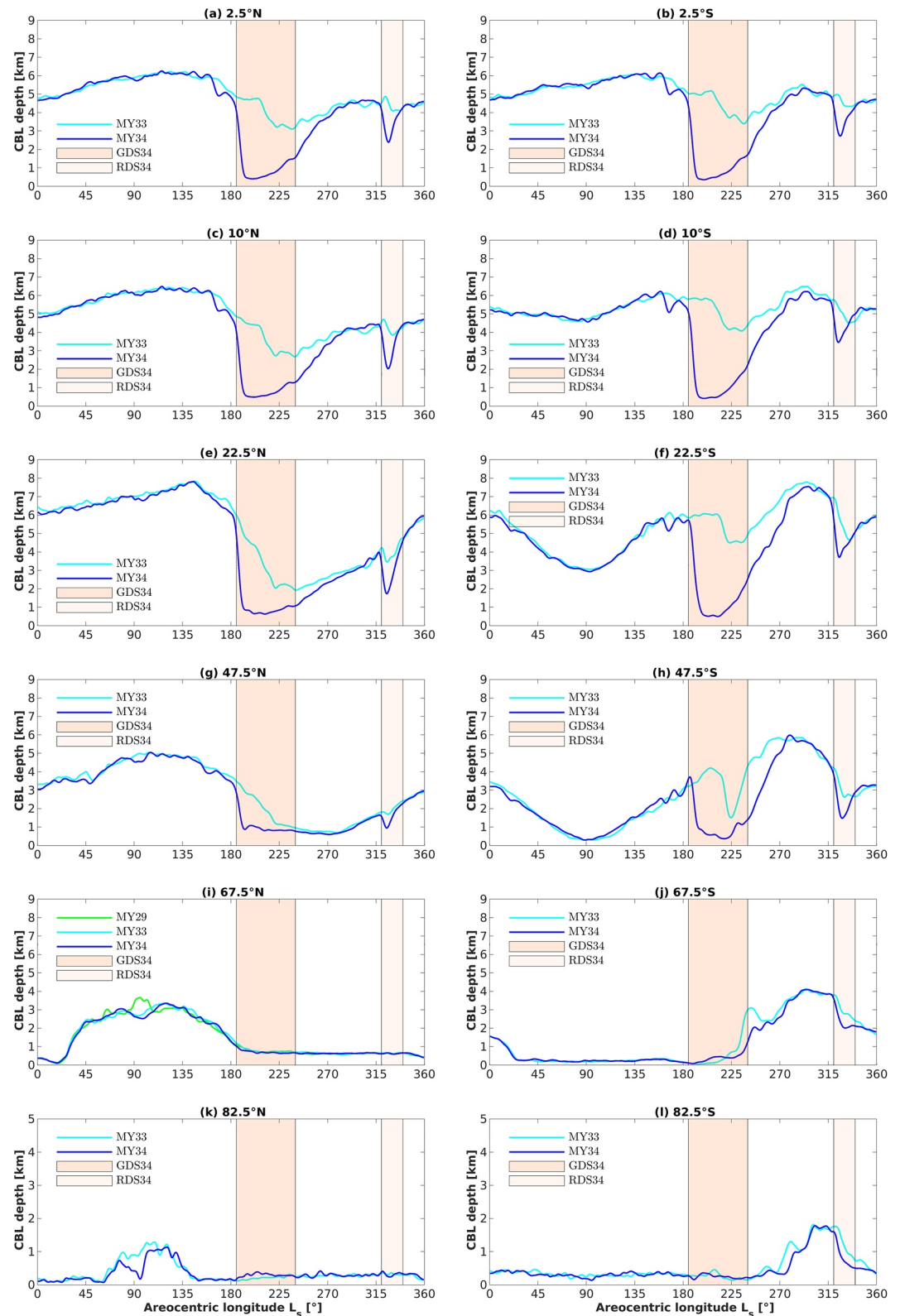 cyan and blue solid lines denote the simulated cases MY 33 and MY 34, respectively. The shaded areas refer to the global dust storms (GDS) in MY 34 (GDS-34) and RDS in MY 34 (RDS-34).

variability in convection velocity (Figure 8c). We examine the zonally averaged depth of the CBL at different latitudes, from the equator up to the polar caps in both hemispheres, for both MY 33 and MY 34 as a function of season (Figure 9). The predicted latitudinal variability in CBL depth indicates that GDS-34-induced suppression in boundary layer activity occurs mostly over the southern hemisphere, which had higher dust opacities during GDS-34. We obtain a decrease in CBL depth by as much as 5.8 km at $22.5°S$ and 4.8 km at $2.5°S$ for MY 34 (Figures 9f–9b), as compared to a reduction of 5.3 km at $22.5°N$ and 4.3 km at $2.5°N$ (Figures 9e–9a). As GDS-34 drives the tropics more actively, CBL evolution during MY 34 is less affected over the high latitudes, especially in the northern hemisphere. For instance, we observe that at $47.5°N$ the CBL drops by 1.9 km (Figure 9g), while it decreases by 3.2 km over $47.5°S$ (Figure 9h). It is worth noting that our CBL depth estimation at the latitude of $67.5°N$ (passing through the Phoenix landing site) is around 3.5 km in northern early summer ($L_s \sim 100°$), as displayed in Figure 9i for MY29. This prediction is consistent with the light detection and ranging instrument (LIDAR) observations of NASA's Phoenix Mars Lander, in which the daytime CBL depth is obtained to be around 4 km (Whiteway et al., 2009). Regarding CBL evolution around the polar caps, we compare MY 33 and MY 34 poleward of 80° in Figures 9k and 9l. Our results indicate that very shallow boundary layers surround the polar caps in both hemispheres (i.e., up to only a few tens of meters), implying the existence of vSBL formation similar to what is observed in terrestrial polar regions (Grachev et al., 2005), associated with very weak turbulence and strong stratification (Banta, 2008; Mahrt & Vickers, 2006), which, in turn, excessively weakens the depth of CBL. In terms of the CBL maxima, Figures 9k and 9l reveal that the CBL depth around the northern polar cap reaches nearly 1.1 km in the northern early summer, while for the southern polar cap, it extends somewhat higher, to ~1.9 km during the southern late-summer. Lastly, even though the dust activity has no effect on the boundary layer over the northern polar cap (Figure 9k), the regional dust storm in MY 34 (RDS-34) produces a gradual response on the extent of boundary layer formation around the southern polar cap. Fig. 9l shows that the boundary layer in MY 34 is lowered by nearly 0.5 km, by the impact of RDS-34.

4.3. Comparison With MEX RO Measurements

We compare the GCM predictions with available MEX radio occultation (RO) measurements of CBL depth (Hinson et al., 2008, 2019). For the comparison of CBL depth, the reference experiments consist of 118 RO profiles overall, collected during the northern midspring ($L_s = 34.7 - 69.2°$) and late winter of MY 27 ($L_s = 357.1 - 359.9°$), through the early spring of MY 28 ($L_s = 0.1 - 42.3°$). The latitude, ϕ, longitude, λ, solar longitude, L_s, local terrain elevations, z_s, based on MOLA (Christensen et al., 2001), and in the GCM, as well as local true solar time (LTST), t_l of these RO measurements are listed in Tables A1 and A2, while the spatial distribution is marked on a topographic map of Mars based on Mars Orbiter Laser Altimeter (MOLA) (D. E. Smith et al., 2001) in Figure 10e.

Tables A1 and A2 list the GCM-based CBL depth predictions, $z_{i,GCM}$, with respect to the RO measurements, $z_{i,RO}$, including the mean absolute error (MAE) values at each given RO location. Results indicate that the CBL predictions of the GCM are consistent with the RO measurements, in which the average MAE of z_i is 1.41 km among the 118 RO profiles with a standard deviation of 1.01 km. Indeed, 100 of 118 RO locations exhibit a good agreement with an average MAE of ~1.1 km in terms of CBL depth. Here, the high MAEs appear around northern Xanthe and Margaritifer Terra regions, in which the GCM underpredicts the depth of CBL as being ~5.7 and 6.1 km compared to a depth of ~8.8 and 8.3 km in RO measurements. This can be caused by the reason that both locations are heavily cratered and irregular regions (Dohm et al., 2007; Sato et al., 2010; Thomas et al., 2017), which can induce extensive mesoscale circulations or convective slope winds over the rim slopes. Similarly, underpredictions in CBL depth are also produced over locations, for instance, western and eastern rims of Isidis Planitia (i.e., a large impact basin) as ~3.2–3.6 km and the Valles Marineris rims as ~5.3 km. Along these regions, high CBL depth values in RO measurements can be related to the well-mixed turbulence enhanced over steep rims. Thus, the presence of strong topographical circulations through Isidis rims (Hinson et al., 2019) and canyon rims of Valles Marineris (Spiga & Forget, 2009) can necessitate high-resolution mesoscale modeling with respect to the GCM approach. Another possible reason is that the terrain elevations can be different between the observation and the model (as listed in Tables A1 and A2), and also that even for identical elevations may exhibit differences due to the thermal inertia assumed at the regionally smoothed GCM mesh in comparison with the actual one at the location of the measurement. Figure 10 shows the spatial variation in observed and modeled CBL depths
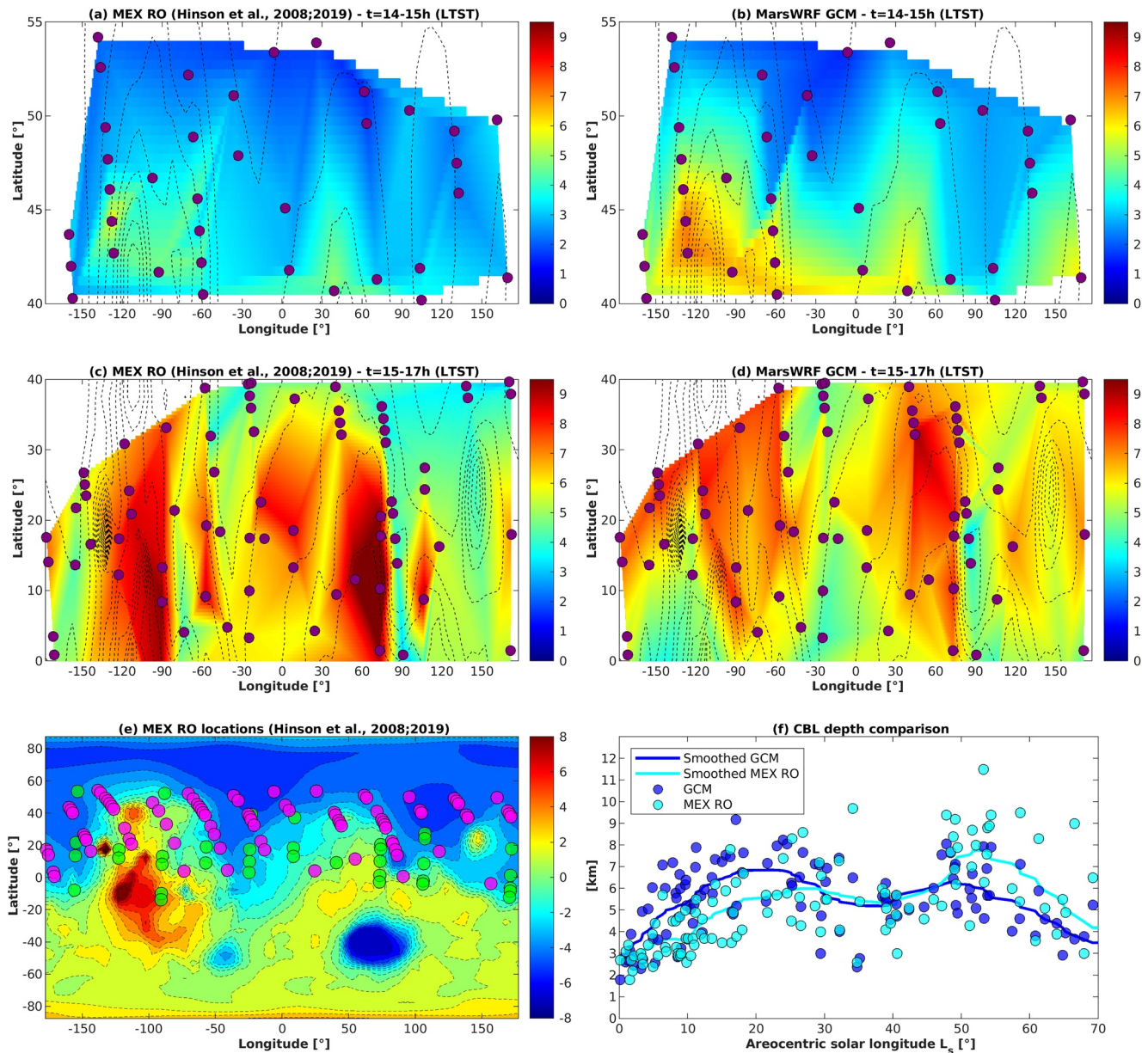
Figure 10. Regional distribution of convective boundary layer (CBL) depth retrieved from Mars express (MEX) radio occultation (RO) measurements (Hinson et al., 2008, 2019) at (a) $t = 14–15$ h (LTST), (c) $t = 15–17$ h (LTST) and MarsWRF general circulation model (GCM) simulations at (b) $t = 14–15$ h (LTST), and (d) $t = 15–17$ h (LTST) for given RO profiles as listed in Tables A1 and A2. The locations of RO experiments are marked with purple circles. The black dashed lines display the contour lines of the topographic map of Mars retrieved by the data sets of Mars Orbiter Laser Altimeter (MOLA) (D. E. Smith et al., 2001). (e) The RO locations are also depicted together with the MOLA map. Here, the green and magenta circles mark the RO profiles collected at MY 27 and MY 28, respectively. (f) The temporal variation of CBL depth is displayed at all available RO locations during northern early and late spring of MY 27 and MY 28. The dark and light blue markers show the GCM and RO results, respectively, while the solid lines display their smoothed behavior through Gaussian smoothing.

at the times of the RO observations using the results shown in Tables A1 and A2. Note that the sharp edges here are due to variations in the L_s and LTST of different RO observations, as well as the lack of RO profiles, especially in the southern tropics. The RO locations are scattered mostly around the northern midlatitudes (Figures 10a and 10b) at $t = 14–15$ h (LTST) and through the northern tropics (Figures 10c and 10d) at $t = 15–17$ h (LTST). The contours of CBL depth predictions derived from the GCM show a spatial variation generally consistent with that of the RO measurements. The deep CBL formations around the high terrains over northern tropics exist in both GCM and RO results. To illustrate, deeper layers mostly appear in the vicinity of Olympus Mons, Tharsis Montes, Valles Marineris, and Syrtis Major, increasing to a depth as great

as ∼7–9 km (Figures 10c and 10d). By contrast, relatively shallower layers form in the northern midlatitudes (e.g., λ ∼40–54°N), largely due to all RO observations being made during northern late winter and early to midspring, when surface heating is lowest at these latitudes (see Section 4.1). The depth of the observed CBL in this region varies from ∼3–7 km with the GCM predicting ∼1.5 km greater depths, but, overall, the general spatial variation here matches well between the GCM and RO results, such as in Arcadia Planitia, Tempe Terra, Acidalia Planitia, and Utopia Planitia (Figures 10a and 10b). Furthermore, in Figure 10f, we compare our GCM estimations with MEX RO measurements in terms of the temporal variation from early to late northern spring ($L_s = 0.1 - 69.7°$). Note that in this figure, we combine the RO profiles of MY 27 and MY 28, as there is little interannual change in the northern spring season due to the lack of strong dust storms or planetary wave activity. For this season, Hinson et al. (2008) reports that the MGS TES observations of dust column opacity (at 9 μm wavelength) in the southern and northern tropics are as low as ∼ 0.05 and 0.1, respectively. The profiles in Figure 10f show a very general agreement between the seasonal variation of predicted and observed CBL depths in northern spring, insofar as both increase rapidly after equinox, have some briefly smaller values midway through the period shown, then increase again before decreasing rapidly toward L_s ∼ 70°. However, as shown by the smoothed curves (through Gaussian-weighted moving averaging [Horová et al., 2012], based on Gaussian distribution-, with a window length of 30, in which the window slides through 30 neighboring elements for a given element), the GCM appears to have a positive bias of nearly 1.0–1.5 km magnitude in northern early spring ($L_s = 0 - 30°$), which reverses to a negative bias of nearly 1.5–2.0 km magnitude in around northern midspring ($L_s = 40 - 70°$). It is worth noting that the latter bias is caused by the local true solar times of corresponding RO observations. To illustrate, most of the RO profiles within this period are retrieved after $t = 17$h (LTST), standing for the "early-evening transition" period, which is challenging to model adequately (Nadeau et al., 2011). This is because, during the early-evening transition, convective boundary layers (characterized by positive surface buoyancy fluxes, that is, unstable regime) begin to convert into stable boundary layers (i.e., surface buoyancy fluxes are reversed to be negative). From terrestrial studies (Busse & Knupp, 2012; Lampert et al., 2016; Pino et al., 2006), early-evening transition of unstable to stable regimes (i.e., large-scale turbulent convections into small-scale sporadically turbulent stratification [Stull, 2012]) are quite dynamic processes where the convective turbulence and radiative heating decays substantially in short periods. Thus, capturing well this time-varying process in GCM can be possible by either implementing external parameterization (Nadeau et al., 2011) or refining model resolutions, which will be taken into account as a future work. In addition, considering the possible model-based or experimental uncertainties and recalling that 100 of 118 RO locations give an average MAE of ∼1 km in terms of CBL depth, the GCM appears to be largely consistent with the radio occultation measurements at the observation times and locations. Lastly, as the available data sets for MEX radio occultation measurements are limited, we cannot examine the potential interannual variabilities in this comparison.

5. Summary and Conclusion

The present study addresses decade-long spatio-temporal variabilities (interannual, seasonal, and regional) in the Martian convective boundary layer. During this period, from MY 24 to MY 34, there have been three major planet-encircling dust events recorded. To examine their impact on CBL characteristics as well as the spatio-temporal variations occurring in the convective boundary layer, we performed a decade-long GCM simulation using the MarsWRF model (Richardson et al., 2007). As the dust cycle is the main driver of boundary layer dynamics, we built a new dust transport scheme in order to correctly represent the time-evolving dust distribution. In our scheme, the dust is transported freely, then corrected by the observed column dust opacity measurements from Montabone et al. (2015); Montabone et al. (2020) as a novel semi-interactive framework. As noted before, several different atmospheric models use different dust interaction schemes, ranging from simple prescribed dust opacity forcings (Forget et al., 1999) to orbit-spin coupling methods using fully interactive dust transport (Newman, Lee, et al., 2019). Here, we did not quantify the possible consequences of using different dust schemes on the boundary-layer meteorology of Mars, which would require extensive high-resolution in situ near-surface meteorological observations. Currently, such a meteorological data set is available by the InSight lander and will be available by the Perseverance rover. A multimodel intercomparison study, covering different dust schemes, is essential as a future work to further improve our understanding of the Martian dust cycle and boundary-layer meteorology. However,

for this study, such an extensive study is out of our current scope. Results of our GCM simulations reveal that enhanced dust content in the Martian atmosphere (especially during global dust storms) has significant impacts on the seasonal and interannual variability in CBL dynamics. We find that a strong reduction in surface convective heat flux occurs for all the global dust storm events recorded during MY 25, MY 28, and MY 34, which is quite unlike the intervening, quiescent Martian years. However, only the global dust storms of MY 25 and MY 34 were able to terminate the convective heat production at a global level. In this manner, both planet-encircling storms reversed the thermal convection process into a prolonged surface cooling, reducing its global average from ~0.35 Km/s at storm onset to below 0 Km/s at the storm's peak (L_s ~ 210°). This surface cooling existed for nearly 95 and 82 sols when GDS-25 and GDS-34 events occur. The suppression in heating rates through GDS events breaks down the daytime convection activity, eliminating deep thermal plumes and intense convective vortices. Accordingly, we find that the velocity scale of turbulent convection was globally lowered, for instance the convective velocity decreases by ~2.5 m/s during GDS-25 and GDS-34, from ~3 m/s at the onset of the storm along the equator (i.e., down to the typical values encountered on Earth's daytime CBL). The global weakening in convective activity was further amplified by enhanced dust transport during the dust storm season (after L_s ~ 180°), inducing higher wind shear on average by almost 50%. The equatorial friction velocity grows from ~0.75 m/s (prior to storm onset) up to ~1.1–1.2 m/s within the dust storm season for each simulated Martian year. As a combination of both impacts, the CBL depth experienced a drop down to as shallow as ~0.5 km, from as high as 9 km at the onsets of GDS-25 and GDS-34. Both storms led to the conversion of deep convective boundary layers into extremely shallow daytime boundary layers, even during the daytime at all local times. As a result, the planet was exposed to a long-term "global-darkness" state, in which its most extreme period (i.e., the number of sols with a CBL depth below 1 km) lasted for nearly 67 and 57 sols during GDS-25 and GDS-34, respectively. On the contrary, the less intense GDS in MY28 differed from its counterparts in MY25 and MY34. It could not negate surface kinematic heat flux globally, even at the storm's peak. Thus, the GDS-28 could not feature extremely shallow daytime boundary layers over the whole planet as long-lasting as in GDS-25 and GDS-34 events. Besides the seasonal and interannual variability, we observed significant impacts on the CBL dynamics governed by regional features. For the Martian CBL, the positive feedback of higher terrain elevation has been well documented from the MEX radio occultation measurements. Consistent with this effect, our GCM simulations point out the existence of other factors that affect the convective boundary layer, such as the GDS-induced dust abundance and inverse contribution of thermal inertia. Regarding the latter effect, our GCM results showed that the lower thermal inertia enhances the turbulent convection, thus leading to deep CBL formation (such as in Amazonis Planitia, Arabia Terra, Alba Patera, and Elysium Mons), while relatively shallow CBLs are found over the tropics, that is, ~5 km, in the Elysium Planitia, Xanthe Terra, and Valles Marineris regions. In terms of PBL formation over the polar caps, we observed the formation of a very stable boundary layer (vSBL) surrounding both polar caps up to a few tens of meters in depth. Such a regime, as observed in terrestrial polar regions (Grachev et al., 2005), is related to very weak turbulence and strong stratification, as a consequence of the perennial water and CO_2 polar caps, which causes surface temperatures to remain very low. Finally, regarding dust feedback on polar caps, we find that the regional dust storm in MY 34 (RDS-34) exhibits a gradual impact over the southern polar cap, where the depth of the CBL is reduced down to 0.5 km, in comparison with the quiescent MY 33. As a future work, thanks to the ongoing operations of InSight lander as well as MSL and Mars 2020 rover, we will expand the current investigation through detailed comparisons of interannual and seasonal variabilities between GCM and in situ meteorological observations. In the present study, regarding the potential implications of global/regional dust storms, we examine the impacts of these extreme dust events on convective boundary layer dynamics. As a follow-up study, we will focus on the influences of global/regional dust storms on the near-surface turbulent energy, and thus the turbulent exchange of volatiles and tracers between the surface and atmosphere.

Appendix A: GCM Versus MEX RO Measurements in Terms of CBL Depth

CBL predictions retrieved from the GCM are compared with the MEX radio occultation (RO) measurements by Hinson et al. (2008); and Hinson et al. (2019), during the northern spring in MY 27 (RO profiles 1–36), northern late winter in MY 27 (RO profiles 37–42), and northern early spring in MY 28 (RO profiles 43–118). Here, the L_s is the areocentric longitude, ϕ is the northern latitude, λ is the Eastern longitude, z_s is the local

terrain elevations based on MOLA (Christensen et al., 2001), and in the GCM, z_i is the depth of CBL, l_t is the local true solar time. Note that MAE_{z_i} refers to the mean absolute error between the GCM and RO measurements (Tables A1 and A2).

Table A1

Comparison Between General Circulation Model (GCM) Versus Mars Express (MEX) Radio Occultation (RO) Measurements for RO Profiles 1–59

RO	L_s [°]	ϕ [°N]	λ [°E]	$z_{s,MOLA}$	$z_{s,GCM}$	$z_{i,RO}$	$z_{i,GCM}$	MAE_{z_i}	t_l [h]
1	34.7	53.6	206.3	−3.6	−3.7	2.60	2.39	0.21	17.1
2	35.1	52.5	271.7	−1.7	−1.9	5.40	2.78	2.62	17.1
3	39.6	39.5	336.7	−4.5	−4.4	4.40	4.58	0.18	17.1
4	40.5	37.3	9.4	−2.5	−2.5	5.70	5.30	0.40	17.1
5	44.5	27.5	107.0	−4.3	−4.3	4.60	5.15	0.55	17.1
6	45.9	24.4	106.9	−3.9	−3.8	5.50	6.02	0.52	17.1
7	47.1	21.8	205.0	−3.9	−3.8	5.20	7.56	2.36	17.2
8	47.8	20.6	74.0	0.2	0.2	9.40	8.06	1.34	17.2
9	48.4	19.3	303.0	−0.9	−0.9	7.70	7.66	0.04	17.2
10	48.8	18.6	8.4	−1.6	−1.7	8.40	6.45	1.95	17.2
11	49.0	18.0	172.0	−2.2	−2.9	6.90	6.99	0.09	17.2
12	49.1	17.8	73.8	−0.5	0.0	9.20	7.12	2.08	17.2
13	49.2	17.5	335.6	−2.9	−2.9	6.20	5.23	0.97	17.2
14	49.4	17.4	237.5	0.9	1.1	7.90	4.87	3.03	17.2
15	51.2	13.7	204.6	−3.6	−3.6	4.30	5.97	1.67	17.2
16	51.5	13.3	8.2	−1.5	−1.4	7.00	5.57	1.43	17.2
17	51.6	13.3	270.0	1.9	0.8	8.70	6.68	2.02	17.2
18	52.1	12.3	237.2	2.5	2.4	8.00	5.09	2.91	17.2
19	53.2	10.3	73.5	1.0	0.9	11.50	7.95	3.55	17.1
20	53.3	10.0	335.3	−3.1	−2.3	6.30	4.62	1.68	17.1
21	53.7	9.5	40.7	0.6	0.7	7.60	6.93	0.67	17.1
22	53.8	9.2	302.5	−0.6	−0.1	8.80	5.69	3.11	17.1
23	54.1	8.8	106.1	−0.7	−0.9	8.90	5.68	3.22	17.1
24	54.3	8.4	269.8	1.8	2.7	9.40	7.92	1.48	17.1
25	57.4	3.3	335.0	−2.8	−2.3	6.00	4.03	1.97	17.1
26	58.5	1.5	171.3	−3.0	−3.0	5.40	4.61	0.79	17.1
27	58.6	1.5	73.1	1.5	1.5	9.50	7.13	2.37	17.1
28	60.8	−1.9	105.7	0.3	−0.3	3.60	3.82	0.22	17.1
29	61.3	−2.5	73.0	1.9	1.7	8.30	5.90	2.40	17.1
30	62.2	−3.9	105.6	0.1	0.3	5.10	4.60	0.50	17.1
31	63.9	−6.4	171.0	−2.9	−2.2	3.90	4.40	0.50	17.1
32	64.8	−7.6	203.8	−1.1	−0.9	5.50	2.93	2.57	17.1
33	65.2	−8.3	171.0	−2.8	−1.9	4.90	3.96	0.94	17.1
34	66.5	−9.7	269.2	4.3	4.1	9.00	3.67	5.33	17.0
35	67.9	−12.1	170.7	−1.8	−1.8	3.00	3.80	0.80	17.0
36	69.2	−13.5	268.9	5.4	5.5	6.50	5.25	1.25	17.0
37	357.1	54.2	221.7	−3.0	−2.9	2.10	2.30	0.20	14.0
38	357.4	53.9	25.7	−3.9	−4.0	1.70	2.45	0.75	14.1

Table A1
Continued

RO	L_s [°]	ϕ [°N]	λ [°E]	$z_{s,MOLA}$	$z_{s,GCM}$	$z_{i,RO}$	$z_{i,GCM}$	MAE_{z_i}	t_l [h]
39	358.0	53.4	353.7	−4.8	−4.8	1.70	1.47	0.23	14.1
40	358.7	52.6	223.6	−2.8	−2.9	2.20	2.72	0.52	14.2
41	359.1	52.2	289.5	−3.5	−2.6	2.10	2.35	0.25	14.2
42	359.9	51.3	61.5	−3.6	−3.5	1.50	2.76	1.26	14.3
43	0.1	51.1	323.5	−4.7	−4.6	2.70	1.79	0.91	14.3
44	0.9	50.3	95.3	−4.6	−4.7	3.10	2.61	0.49	14.3
45	1.3	49.8	161.3	−3.8	−3.7	3.40	2.69	0.71	14.4
46	1.5	49.6	63.3	−3.5	−3.4	1.80	3.14	1.34	14.4
47	1.7	49.4	227.2	−2.4	−2.2	2.70	3.90	1.20	14.4
48	1.9	49.2	129.2	−4.7	−4.7	2.20	2.87	0.67	14.4
49	2.1	48.9	293.1	−1.5	−1.6	2.90	2.46	0.44	14.4
50	3.1	47.9	327.0	−4.5	−4.6	3.00	2.31	0.69	14.5
51	3.3	47.7	228.9	−2.0	−2.3	2.80	4.94	2.14	14.5
52	3.4	47.5	130.8	−4.7	−4.5	2.50	2.73	0.23	14.5
53	4.2	46.7	262.6	−0.3	−0.3	3.40	5.07	1.67	14.6
54	4.8	46.1	230.5	−1.7	−1.3	3.90	6.05	2.15	14.6
55	4.9	45.9	132.4	−4.7	−4.6	2.40	3.71	1.31	14.6
56	5.2	45.6	296.3	−1.1	−1.5	4.40	2.57	1.83	14.6
57	5.6	45.1	2.2	−4.2	−4.3	2.90	3.64	0.74	14.7
58	6.3	44.4	232.0	−1.1	−0.7	5.70	7.10	1.40	14.7
59	6.7	43.9	297.8	−1.5	−1.1	3.30	6.02	2.72	14.7

Table A2
Comparison Between General Circulation Model (GCM) Versus Mars Express (MEX) Radio Occultation (RO) Measurements for RO Profiles 60–118

RO	L_s [°]	ϕ [°N]	λ [°E]	$z_{s,MOLA}$	$z_{s,GCM}$	$z_{i,RO}$	$z_{i,GCM}$	MAE_{z_i}	t_l [h]
60	6.8	43.7	199.8	−4.0	−4.0	3.10	3.88	0.78	14.7
61	7.8	42.7	233.5	−0.3	−0.8	4.50	7.20	2.70	14.8
62	8.2	42.2	299.3	−1.2	−1.1	4.50	5.80	1.30	14.8
63	8.3	42.0	201.3	−3.9	−3.9	3.30	5.56	2.26	14.8
64	8.5	41.9	103.2	−5.0	−4.9	3.00	2.85	0.15	14.8
65	8.6	41.8	5.2	−3.8	−3.1	2.90	4.66	1.76	14.9
66	8.8	41.7	267.1	0.5	0.3	4.70	6.65	1.95	14.9
67	8.9	41.4	169.1	−3.8	−3.5	2.90	6.00	3.10	14.9
68	9.0	41.3	71.0	−3.1	−3.0	3.00	3.25	0.25	14.9
69	9.6	40.7	38.8	−1.6	−1.8	5.00	6.18	1.18	14.9
70	9.7	40.5	300.6	−1.2	−1.6	3.70	6.40	2.70	14.9
71	9.8	40.3	202.7	−3.9	−3.9	2.60	5.22	2.62	14.9
72	10.0	40.2	104.5	−5.0	−4.9	3.70	3.68	0.02	14.9
73	10.4	39.7	170.4	−3.9	−3.9	2.90	5.06	2.16	15.0
74	10.7	39.4	334.2	−4.5	−4.4	3.70	4.40	0.70	15.0
75	10.9	39.1	138.1	−4.3	−4.3	3.40	5.27	1.87	15.0

Table A2
Continued

RO	L_s [°]	ϕ [°N]	λ [°E]	$z_{s,MOLA}$	$z_{s,GCM}$	$z_{i,RO}$	$z_{i,GCM}$	MAE_{z_i}	t_l [h]
76	11.1	39.0	40.0	−0.9	−1.2	4.90	6.99	2.09	15.0
77	11.2	38.8	301.9	−1.7	−1.5	5.50	7.90	2.40	15.0
78	11.9	38.0	171.6	−3.9	−3.9	3.90	5.67	1.77	15.0
79	12.1	37.7	335.5	−4.4	−4.5	4.60	3.97	0.63	15.0
80	12.4	37.4	139.3	−4.2	−4.2	3.70	5.96	2.26	15.1
81	13.5	36.2	74.7	−2.6	−2.0	3.70	6.52	2.82	15.1
82	13.6	36.0	336.6	−4.3	−4.3	5.40	5.77	0.37	15.1
83	14.0	35.6	42.3	0.0	−0.3	6.20	7.36	1.16	15.1
84	15.0	34.5	75.8	−2.6	−2.6	3.50	7.24	3.74	15.2
85	15.5	33.9	43.4	−0.2	−0.5	5.90	7.55	1.65	15.2
86	16.2	33.2	272.9	0.7	0.8	7.80	7.47	0.33	15.2
87	16.4	32.8	76.8	−2.4	−2.5	3.50	4.93	1.43	15.3
88	16.6	32.6	338.7	−4.0	−4.1	4.90	4.83	0.07	15.3
89	17.0	32.2	44.4	−0.9	−0.7	6.30	9.18	2.88	15.3
90	17.1	32.0	306.2	−3.1	−3.2	3.80	5.21	1.41	15.3
91	17.9	31.1	77.7	−1.6	−2.3	4.10	6.74	2.64	15.3
92	18.1	30.9	241.5	2.0	2.3	6.70	7.66	0.96	15.3
93	21.4	26.9	309.0	−3.7	−3.1	5.70	5.41	0.29	15.5
94	21.6	26.8	210.9	−3.4	−2.9	4.90	7.17	2.27	15.5
95	23.0	25.1	211.8	−3.0	−2.9	5.70	7.98	2.28	15.5
96	23.9	24.2	245.0	2.4	2.9	7.40	8.24	0.84	15.6
97	24.5	23.5	212.7	−3.1	−2.7	5.80	8.06	2.26	15.6
98	25.1	22.7	82.1	−2.2	−2.3	4.50	6.26	1.76	15.6
99	25.2	22.6	344.0	−1.9	−2.6	8.30	6.14	2.16	15.6
100	26.3	21.4	279.1	−0.1	0.0	5.60	6.53	0.93	15.6
101	26.5	21.0	83.0	−2.9	−2.5	4.30	5.17	0.87	15.6
102	26.8	20.9	246.8	2.5	2.6	8.60	7.67	0.93	15.7
103	28.6	18.4	313.3	−3.5	−3.3	5.20	7.14	1.94	15.7
104	29.2	17.6	182.8	−3.3	−3.3	7.20	7.09	0.11	15.7
105	29.4	17.4	84.7	−3.7	−3.8	4.00	3.01	0.99	15.7
106	29.5	17.4	346.6	−1.7	−2.3	6.60	4.75	1.85	15.7
107	30.1	16.6	216.1	−2.2	−2.0	5.50	6.32	0.82	15.8
108	30.3	16.3	117.9	−3.2	−3.3	5.50	6.95	1.45	15.7
109	32.1	14.1	184.4	−3.2	−3.1	7.30	7.42	0.12	15.8
110	32.2	13.9	86.3	−3.8	−3.8	4.10	4.02	0.08	15.8
111	34.1	11.6	54.7	1.4	1.4	9.70	6.51	3.19	15.8
112	38.4	4.8	318.7	−1.3	−1.1	6.00	5.64	0.36	15.9
113	38.8	4.3	24.4	0.2	0.1	5.80	5.59	0.21	15.9
114	38.9	4.1	286.2	1.4	1.9	4.10	6.25	2.15	15.9
115	39.0	3.5	188.1	−3.2	−3.0	5.10	5.40	0.30	15.9
116	40.4	0.9	188.7	−2.9	−2.8	4.80	5.67	0.87	15.9
117	40.6	0.9	90.6	−0.4	−0.2	3.00	4.73	1.73	15.9
118	42.3	−3.6	156.5	−2.3	−2.4	5.10	5.02	0.08	15.9

Data Availability Statement

The data of MarsWRF GCM simulations between Mars Years 24 and 34 as well as the model-observation comparisons presented in this research are available online at https://doi.org/10.17605/OSF.IO/MU6J8 (Senel, 2021).

References

Aoki, S., Vandaele, A., Daerden, F., Villanueva, G., Liuzzi, G., Thomas, I., et al. (2019). Water vapor vertical profiles on Mars in dust storms observed by TGO/NOMAD. *Journal of Geophysical Research: Planets*, *124*(12), 3482–3497. https://doi.org/10.1029/2019je006109

Banfield, D., Spiga, A., Newman, C., Forget, F., Lemmon, M., Lorenz, R., et al. (2020). The atmosphere of Mars as observed by InSight. *Nature Geoscience*, *13*, 1–9.

Banta, R. M. (2008). Stable-boundary-layer regimes from the perspective of the low-level jet. *Acta Geophysica*, *56*(1), 58–87. https://doi.org/10.2478/s11600-007-0049-8

Basu, S., Wilson, J., Richardson, M., & Ingersoll, A. (2006). Simulation of spontaneous and variable global dust storms with the GFDL Mars GCM. *Journal of Geophysical Research*, *111*(E9). https://doi.org/10.1029/2005je002660

Bertrand, T., Wilson, R., Kahre, M., Urata, R., & Kling, A. (2020). Simulation of the 2018 global dust storm on Mars using the NASA Ames Mars GCM: A multitracer approach. *Journal of Geophysical Research: Planets*, *125*(7), e2019JE006122. https://doi.org/10.1029/2019je006122

Brooks, I. M., & Fowler, A. M. (2012). An evaluation of boundary-layer depth, inversion and entrainment parameters by large-eddy simulation. *Boundary-Layer Meteorology*, *142*(2), 245–263. https://doi.org/10.1007/s10546-011-9668-3

Busse, J., & Knupp, K. (2012). Observed characteristics of the afternoon–evening boundary layer transition based on sodar and surface data. *Journal Of Applied Meteorology and Climatology*, *51*(3), 571–582. https://doi.org/10.1175/2011jamc2607.1

Christensen, P. R., Bandfield, J. L., Hamilton, V. E., Ruff, S. W., Kieffer, H. H., Titus, T. N., et al. (2001). Mars Global Surveyor Thermal Emission Spectrometer experiment: Investigation description and surface science results. *Journal of Geophysical Research*, *106*(E10), 23823–23871. https://doi.org/10.1029/2000je001370

Christensen, P. R., Jakosky, B. M., Kieffer, H. H., Malin, M. C., McSween, H. Y., Nealson, K., et al. (2004). The thermal emission imaging system (THEMIS) for the Mars 2001 Odyssey Mission. *Space Science Reviews*, *110*(1–2), 85–130. https://doi.org/10.1007/978-0-306-48600-5_3

Colaïtis, A., Spiga, A., Hourdin, F., Rio, C., Forget, F., & Millour, E. (2013). A thermal plume model for the Martian convective boundary layer. *Journal of Geophysical Research*, *118*(7), 1468–1487. https://doi.org/10.1002/jgre.20104

Conrath, B. J. (1975). Thermal structure of the Martian atmosphere during the dissipation of the dust storm of 1971. *Icarus*, *24*(1), 36–46. https://doi.org/10.1016/0019-1035(75)90156-6

Davy, R., Davis, J. A., Taylor, P. A., Lange, C. F., Weng, W., Whiteway, J., & Gunnlaugson, H. P. (2010). Initial analysis of air temperature and related data from the Phoenix MET station and their use in estimating turbulent heat fluxes. *Journal of Geophysical Research*, *115*(E3). https://doi.org/10.1029/2009je003444

Deardorff, J. W. (1970). Convective velocity and temperature scales for the unstable planetary boundary layer and for Rayleigh convection. *Journal of the Atmospheric Sciences*, *27*(8), 1211–1213. https://doi.org/10.1175/1520-0469(1970)027<1211:cvatsf>2.0.co;2

Dohm, J. M., Barlow, N. G., Anderson, R. C., Williams, J.-P., Miyamoto, H., Ferris, J. C., et al. (2007). Possible ancient giant basin and related water enrichment in the Arabia Terra province, Mars. *Icarus*, *190*(1), 74–92. https://doi.org/10.1016/j.icarus.2007.03.006

Fedorova, A. A., Montmessin, F., Korablev, O., Luginin, M., Trokhimovskiy, A., Belyaev, D. A., et al. (2020). Stormy water on Mars: The distribution and saturation of atmospheric water during the dusty season. *Science*, *367*(6475), 297–300. https://doi.org/10.1126/science.aay9522

Fonseca, R. M., Zorzano-Mier, M.-P., & Martín-Torres, J. (2018). Planetary boundary layer and circulation dynamics at gale crater, Mars. *Icarus*, *302*, 537–559. https://doi.org/10.1016/j.icarus.2017.11.036

Forget, F., Hourdin, F., Fournier, R., Hourdin, C., Talagrand, O., Collins, M., et al. (1999). Improved general circulation models of the Martian atmosphere from the surface to above 80 km. *Journal of Geophysical Research*, *104*(E10), 24155–24175. https://doi.org/10.1029/1999je001025

Forget, F., & Montabone, L. (2017). Atmospheric dust on Mars: A review. In *47th international conference on environmental systems*. Charleston, SC.

Fueten, F., Stesky, R. M., & MacKinnon, P. (2005). Structural attitudes of large scale layering in Valles Marineris, Mars, calculated from Mars Orbiter Laser Altimeter data and Mars Orbiter Camera imagery. *Icarus*, *175*(1), 68–77. https://doi.org/10.1016/j.icarus.2004.11.010

Gheynani, B. T., & Taylor, P. A. (2010). Large-eddy simulations of vertical vortex formation in the terrestrial and Martian convective boundary layers. *Boundary-Layer Meteorology*, *137*(2), 223–235. https://doi.org/10.1007/s10546-010-9530-z

Grachev, A. A., Fairall, C. W., Persson, P. O. G., Andreas, E. L., & Guest, P. S. (2005). Stable boundary-layer scaling regimes: The SHEBA data. *Boundary-Layer Meteorology*, *116*(2), 201–235. https://doi.org/10.1007/s10546-004-2729-0

Greybush, S. J., Wilson, R. J., Hoffman, R. N., Hoffman, M. J., Miyoshi, T., Ide, K., & Kalnay, E. (2012). Ensemble Kalman filter data assimilation of thermal emission spectrometer temperature retrievals into a Mars GCM. *Journal of Geophysical Research*, *117*(E11). https://doi.org/10.1029/2012je004097

Guo, X., Lawson, W. G., Richardson, M. I., & Toigo, A. (2009). Fitting the Viking lander surface pressure cycle with a Mars general circulation model. *Journal of Geophysical Research*, *114*(E7). https://doi.org/10.1029/2008je003302

Guzewich, S. D., Lemmon, M., Smith, C., Martínez, G., de Vicente-Retortillo, Á., Newman, C., et al. (2019). Mars Science Laboratory observations of the 2018/Mars year 34 global dust storm. *Geophysical Research Letters*, *46*(1), 71–79. https://doi.org/10.1029/2018gl080839

Guzewich, S. D., Newman, C., Smith, M., Moores, J., Smith, C., Moore, C., et al. (2017). The vertical dust profile over Gale crater, Mars. *Journal of Geophysical Research: Planets*, *122*(12), 2779–2792. https://doi.org/10.1002/2017je005420

Guzewich, S. D., Talaat, E. R., Toigo, A. D., Waugh, D. W., & McConnochie, T. H. (2013). High-altitude dust layers on Mars: Observations with the Thermal Emission Spectrometer. *Journal of Geophysical Research*, *118*(6), 1177–1194. https://doi.org/10.1002/jgre.20076

Guzewich, S. D., Toigo, A. D., Richardson, M. I., Newman, C. E., Talaat, E. R., Waugh, D. W., & McConnochie, T. H. (2013). The impact of a realistic vertical dust distribution on the simulation of the Martian general circulation. *Journal of Geophysical Research*, *118*(5), 980–993. https://doi.org/10.1002/jgre.20084

Haberle, R. M., Leovy, C. B., & Pollack, J. B. (1982). Some effects of global dust storms on the atmospheric circulation of Mars. *Icarus*, *50*(2–3), 322–367. https://doi.org/10.1016/0019-1035(82)90129-4

Haberle, R. M., Pollack, J. B., Barnes, J. R., Zurek, R. W., Leovy, C. B., Murphy, J. R., & Schaeffer, J. (1993). Mars atmospheric dynamics as simulated by the NASA Ames General Circulation model: 1. the zonal-mean circulation. *Journal of Geophysical Research*, *98*(E2), 3093–3123. https://doi.org/10.1029/92je02946

Hamilton, V. E., Vasavada, A. R., Sebastián, E., de la Torre Juarez, M., Ramos, M., Armiens, C., et al. (2014). Observations and preliminary science results from the first 100 sols of MSL Rover Environmental Monitoring Station ground temperature sensor measurements at Gale crater. *Journal of Geophysical Research: Planets*, *119*(4), 745–770. https://doi.org/10.1002/2013je004520

Heavens, N., Richardson, M., Kleinböhl, A., Kass, D., McCleese, D., Abdou, W., & Wolkenberg, P. (2011a). Vertical distribution of dust in the Martian atmosphere during northern spring and summer: High-altitude tropical dust maximum at northern summer solstice. *Journal of Geophysical Research*, *116*(E1). https://doi.org/10.1029/2010je003692

Heavens, N., Richardson, M., Kleinböhl, A., Kass, D., McCleese, D., Abdou, W., & Wolkenberg, P. (2011b). The vertical distribution of dust in the Martian atmosphere during northern spring and summer: Observations by the Mars Climate Sounder and analysis of zonal average vertical dust profiles. *Journal of Geophysical Research*, *116*(E4). https://doi.org/10.1029/2010je003691

Heffter, J. L. (1980). *Air resources laboratories atmospheric transport and dispersion model (ARL-ATAD) (Tech. Rep.)*. Silver Spring, MD (USA): National Oceanic and Atmospheric Administration.

Hinson, D., Pätzold, M., Tellmann, S., Häusler, B., & Tyler, G. (2008). The depth of the convective boundary layer on Mars. *Icarus*, *198*(1), 57–66. https://doi.org/10.1016/j.icarus.2008.07.003

Hinson, D., Tyler, D., Lewis, S., Pätzold, M., Tellmann, S., Häusler, B., & Tyler, G. (2019). The Martian daytime convective boundary layer: Results from radio occultation measurements and a mesoscale model. *Icarus*, *326*, 105–122. https://doi.org/10.1016/j.icarus.2019.02.028

Horová, I., Kolacek, J., & Zelinka, J. (2012). *Kernel smoothing in MATLAB: Theory and practice of kernel smoothing*. World Scientific.

Hu, X.-M., Nielsen-Gammon, J. W., & Zhang, F. (2010). Evaluation of three planetary boundary layer schemes in the WRF model. *Journal of Applied Meteorology and Climatology*, *49*(9), 1831–1844. https://doi.org/10.1175/2010jamc2432.1

Jiménez, P. A., & Dudhia, J. (2012). Improving the representation of resolved and unresolved topographic effects on surface wind in the WRF model. *Journal of Applied Meteorology and Climatology*, *51*(2), 300–316. https://doi.org/10.1175/jamc-d-11-084.1

Kahre, M., Hollingsworth, J., Haberle, R., & Montmessin, F. (2011). Coupling Mars' dust and water cycles: Effects on dust lifting vigor, spatial extent and seasonality. *Mars atmosphere: Modelling and observation* (pp. 143–146). Laboratoire de Meteorologie Dynamique (LMD).

Kahre, M., Hollingsworth, J., Haberle, R., & Wilson, R. (2015). Coupling the Mars dust and water cycles: The importance of radiative-dynamic feedbacks during northern hemisphere summer. *Icarus*, *260*, 477–480. https://doi.org/10.1016/j.icarus.2014.07.017

Kahre, M., Wilson, R., Haberle, R., & Hollingsworth, J. (2009). *An inverse approach to modeling the dust cycle with two Mars general circulation models* (pp. 125–129). Mars Dust Cycle Workshop Ames Research Center.

Kaimal, J., Wyngaard, J., Haugen, D., Coté, O., Izumi, Y., Caughey, S., & Readings, C. (1976). Turbulence structure in the convective boundary layer. *Journal of the Atmospheric Sciences*, *33*(11), 2152–2169. https://doi.org/10.1175/1520-0469(1976)033<2152:tsitcb>2.0.co;2

Kass, D., Schofield, J., Kleinböhl, A., McCleese, D., Heavens, N., Shirley, J., & Steele, L. (2020). Mars Climate Sounder observation of Mars' 2018 global dust storm. *Geophysical Research Letters*, *47*(23), e2019GL083931. https://doi.org/10.1029/2019gl083931

Kleinböhl, A., Schofield, J. T., Kass, D. M., Abdou, W. A., Backus, C. R., Sen, B., et al. (2009). Mars climate sounder limb profile retrieval of atmospheric temperature, pressure, and dust and water ice opacity. *Journal of Geophysical Research*, *114*(E10). https://doi.org/10.1029/2009je003358

Kleinböhl, A., Spiga, A., Kass, D. M., Shirley, J. H., Millour, E., Montabone, L., & Forget, F. (2020). Diurnal variations of dust during the 2018 global dust storm observed by the Mars Climate Sounder. *Journal of Geophysical Research: Planets*, *125*(1), e2019JE006115. https://doi.org/10.1029/2019je006115

Kosović, B., & Curry, J. A. (2000). A large eddy simulation study of a quasi-steady, stably stratified atmospheric boundary layer. *Journal of the Atmospheric Sciences*, *57*(8), 1052–1068.

Lampert, A., Pätzold, F., Jiménez, M. A., Lobitz, L., Martin, S., Lohmann, G., et al. (2016). A study of local turbulence and anisotropy during the afternoon and evening transition with an unmanned aerial system and mesoscale simulation. *Atmospheric Chemistry and Physics*, *16*(12), 8009–8021. https://doi.org/10.5194/acp-16-8009-2016

Larsen, S. E., Jørgensen, H. E., Landberg, L., & Tillman, J. (2002). Aspects of the atmospheric surface layers on Mars and Earth. *Boundary-Layer Meteorology*, *105*(3), 451–470. https://doi.org/10.1023/a:1020338016753

Lee, C., Lawson, W., Richardson, M., Anderson, J., Collins, N., Hoar, T., & Mischna, M. (2011). Demonstration of ensemble data assimilation for Mars using dart, MarsWRF, and radiance observations from MGS TES. *Journal of Geophysical Research*, *116*(E11). https://doi.org/10.1029/2011je003815

Lee, C., Richardson, M. I., Newman, C. E., & Mischna, M. A. (2018). The sensitivity of solstitial pauses to atmospheric ice and dust in the MarsWRF general circulation model. *Icarus*, *311*, 23–34. https://doi.org/10.1016/j.icarus.2018.03.019

Lewis, S. R., Collins, M., Read, P. L., Forget, F., Hourdin, F., Fournier, R., & Huot, J.-P. (1999). A climate database for Mars. *Journal of Geophysical Research*, *104*(E10), 24177–24194. https://doi.org/10.1029/1999je001024

Liu, J., Richardson, M. I., & Wilson, R. (2003). An assessment of the global, seasonal, and interannual spacecraft record of Martian climate in the thermal infrared. *Journal of Geophysical Research*, *108*(E8). https://doi.org/10.1029/2002je001921

Liuzzi, G., Villanueva, G. L., Crismani, M. M., Smith, M. D., Mumma, M. J., Daerden, F., et al. (2020). Strong variability of Martian water ice clouds during dust storms revealed from ExoMars Trace Gas Orbiter/NOMAD. *Journal of Geophysical Research: Planets*, *125*(4), e2019JE006250. https://doi.org/10.1029/2019je006250

Madeleine, J.-B., Forget, F., Millour, E., Montabone, L., & Wolff, M. (2011). Revisiting the radiative impact of dust on Mars using the LMD global climate model. *Journal of Geophysical Research*, *116*(E11). https://doi.org/10.1029/2011je003855

Madeleine, J.-B., Forget, F., Millour, E., Navarro, T., & Spiga, A. (2012). The influence of radiatively active water ice clouds on the Martian climate. *Geophysical Research Letters*, *39*(23). https://doi.org/10.1029/2012gl053564

Mahrt, L., & Vickers, D. (2006). Extremely weak mixing in stable conditions. *Boundary-Layer Meteorology*, *119*(1), 19–39. https://doi.org/10.1007/s10546-005-9017-5

Martin, L. J., & Zurek, R. W. (1993). An analysis of the history of dust activity on Mars. *Journal of Geophysical Research*, *98*(E2), 3221–3246. https://doi.org/10.1029/92je02937

Martínez, G., Valero, F., & Vázquez, L. (2009). Characterization of the Martian convective boundary layer. *Journal of the Atmospheric Sciences*, *66*(7), 2044–2058. https://doi.org/10.1175/2009jas3007.1

Mason, P., & Derbyshire, S. (1990). Large-eddy simulation of the stably-stratified atmospheric boundary layer. *Boundary-Layer Meteorology*, *53*(1–2), 117–162. https://doi.org/10.1007/bf00122467

McCleese, D., Heavens, N., Schofield, J., Abdou, W., Bandfield, J., Calcutt, S., et al. (2010). Structure and dynamics of the Martian lower and middle atmosphere as observed by the Mars Climate Sounder: Seasonal variations in zonal mean temperature, dust, and water ice aerosols. *Journal of Geophysical Research*, *115*(E12). https://doi.org/10.1029/2010je003677

McCleese, D., Schofield, J., Taylor, F., Calcutt, S., Foote, M., Kass, D., & Zurek, R. (2007). Mars Climate Sounder: An investigation of thermal and water vapor structure, dust and condensate distributions in the atmosphere, and energy balance of the polar regions. *Journal of Geophysical Research*, *112*(E5). https://doi.org/10.1029/2006je002790

Michaels, T. I., & Rafkin, S. C. (2004). Large-eddy simulation of atmospheric convection on Mars. *Quarterly Journal of the Royal Meteorological Society*, *130*(599), 1251–1274. https://doi.org/10.1256/qj.02.169

Milkovich, S. M., Head, J. W., & Marchant, D. R. (2006). Debris-covered piedmont glaciers along the northwest flank of the Olympus Mons scarp: Evidence for low-latitude ice accumulation during the Late Amazonian of Mars. *Icarus*, *181*(2), 388–407. https://doi.org/10.1016/j.icarus.2005.12.006

Mischna, M. A., Lee, C., & Richardson, M. (2012). Development of a fast, accurate radiative transfer model for the Martian atmosphere, past and present. *Journal of Geophysical Research*, *117*(E10). https://doi.org/10.1029/2012je004110

Moeng, C.-H., & Sullivan, P. P. (1994). A comparison of shear-and buoyancy-driven planetary boundary layer flows. *Journal of the Atmospheric Sciences*, *51*(7), 999–1022. https://doi.org/10.1175/1520-0469(1994)051<0999:acosab>2.0.co;2

Montabone, L., Forget, F., Millour, E., Wilson, R., Lewis, S., Cantor, B., et al. (2015). Eight-year climatology of dust optical depth on Mars. *Icarus*, *251*, 65–95. https://doi.org/10.1016/j.icarus.2014.12.034

Montabone, L., Spiga, A., Kass, D. M., Kleinböhl, A., Forget, F., & Millour, E. (2020). Martian year 34 column dust climatology from Mars Climate Sounder observations: Reconstructed maps and model simulations. *Journal of Geophysical Research: Planets*, *125*, e2019JE006111. https://doi.org/10.1029/2019je006111

Moores, J. E., Lemmon, M. T., Kahanpää, H., Rafkin, S. C., Francis, R., Pla-Garcia, J., et al. (2015). Observational evidence of a suppressed planetary boundary layer in northern Gale crater, Mars as seen by the Navcam instrument onboard the Mars Science Laboratory rover. *Icarus*, *249*, 129–142. https://doi.org/10.1016/j.icarus.2014.09.020

Morrison, H., & Gettelman, A. (2008). A new two-moment bulk stratiform cloud microphysics scheme in the Community Atmosphere Model, version 3 (CAM3). part i: Description and numerical tests. *Journal of Climate*, *21*(15), 3642–3659. https://doi.org/10.1175/2008jcli2105.1

Nadeau, D. F., Pardyjak, E. R., Higgins, C. W., Fernando, H. J. S., & Parlange, M. B. (2011). A simple model for the afternoon and early evening decay of convective turbulence over different land surfaces. *Boundary-Layer Meteorology*, *141*(2), 301–324. https://doi.org/10.1007/s10546-011-9645-x

Navarro, T., Madeleine, J.-B., Forget, F., Spiga, A., Millour, E., Montmessin, F., & Määttänen, A. (2014). Global climate modeling of the Martian water cycle with improved microphysics and radiatively active water ice clouds. *Journal of Geophysical Research: Planets*, *119*(7), 1479–1495. https://doi.org/10.1002/2013je004550

Neary, L., Daerden, F., Aoki, S., Whiteway, J., Clancy, R. T., Smith, M, et al. (2020). Explanation for the increase in high-altitude water on Mars observed by NOMAD during the 2018 global dust storm. *Geophysical Research Letters*, *47*(7), e2019GL084354. https://doi.org/10.1029/2019gl084354

Newman, C. E., Gómez-Elvira, J., Marin, M., Navarro, S., Torres, J., Richardson, M. I., et al. (2017). Winds measured by the Rover Environmental Monitoring Station (REMS) during the Mars Science Laboratory (MSL) rover's Bagnold Dunes Campaign and comparison with numerical modeling using MarsWRF. *Icarus*, *291*, 203–231. https://doi.org/10.1016/j.icarus.2016.12.016

Newman, C. E., Kahanpää, H., Richardson, M., Martínez, G. M., Vicente-Retortillo, A., & Lemmon, M. (2019). MarsWRF convective vortex and dust devil predictions for Gale crater over 3 Mars years and comparison with MSL-REMS observations. *Journal of Geophysical Research: Planets*, *124*(12), 3442–3468. https://doi.org/10.1029/2019je006082

Newman, C. E., Lee, C., Mischna, M. A., Richardson, M. I., & Shirley, J. H. (2019). An initial assessment of the impact of postulated orbit-spin coupling on Mars dust storm variability in fully interactive dust simulations. *Icarus*, *317*, 649–668. https://doi.org/10.1016/j.icarus.2018.07.023

Newman, C. E., Lewis, S. R., Read, P. L., & Forget, F. (2002). Modeling the Martian dust cycle, 1. Representations of dust transport processes. *Journal of Geophysical Research*, *107*(E12), 6–1. https://doi.org/10.1029/2002je001910

Newman, C. E., & Richardson, M. I. (2015). The impact of surface dust source exhaustion on the Martian dust cycle, dust storms and interannual variability, as simulated by the MarsWRF general circulation model. *Icarus*, *257*, 47–87. https://doi.org/10.1016/j.icarus.2015.03.030

Nielsen-Gammon, J. W., Powell, C. L., Mahoney, M. J., Angevine, W. M., Senff, C., White, A., & Knupp, K. (2008). Multisensor estimation of mixing heights over a coastal city. *Journal of Applied Meteorology and Climatology*, *47*(1), 27–43. https://doi.org/10.1175/2007jamc1503.1

Ordonez-Etxeberria, I., Hueso, R., & Sánchez-Lavega, A. (2018). A systematic search of sudden pressure drops on Gale crater during two Martian years derived from MSL/REMS data. *Icarus*, *299*, 308–330. https://doi.org/10.1016/j.icarus.2017.07.032

Paton, M., Harri, A.-M., & Savijärvi, H. (2018). Measurement of Martian boundary layer winds by the displacement of jettisoned lander hardware. *Icarus*, *309*, 345–362. https://doi.org/10.1016/j.icarus.2018.03.020

Pätzold, M., Häusler, B., Tyler, G., Andert, T., Asmar, S., Bird, M., et al. (2016). Mars express 10 years at Mars: Observations by the Mars Express Radio Science experiment (Mars). *Planetary and Space Science*, *127*, 44–90. https://doi.org/10.1016/j.pss.2016.02.013

Perrin, C., Rodriguez, S., Jacob, A., Lucas, A., Spiga, A., Murdoch, N., et al. (2020). Monitoring of dust devil tracks around the InSight landing site, Mars, and comparison with in situ atmospheric data. *Geophysical Research Letters*, *47*(10), e2020GL087234. https://doi.org/10.1029/2020gl087234

Petrosyan, A., Galperin, B., Larsen, S. E., Lewis, S., Määttänen, A., Read, P., et al. (2011). The Martian atmospheric boundary layer. *Reviews of Geophysics*, *49*(3). https://doi.org/10.1029/2010rg000351

Pino, D., Jonker, H. J., De Arellano, J. V.-G., & Dosio, A. (2006). Role of shear and the inversion strength during sunset turbulence over land: Characteristic length scales. *Boundary-Layer Meteorology*, *121*(3), 537–556. https://doi.org/10.1007/s10546-006-9080-6

Putzig, N. E., & Mellon, M. T. (2007). Apparent thermal inertia and the surface heterogeneity of Mars. *Icarus*, *191*(1), 68–94. https://doi.org/10.1016/j.icarus.2007.05.013

Putzig, N. E., Mellon, M. T., Kretke, K. A., & Arvidson, R. E. (2005). Global thermal inertia and surface properties of Mars from the MGS mapping mission. *Icarus*, *173*(2), 325–341. https://doi.org/10.1016/j.icarus.2004.08.017

Rennó, N. O., Abreu, V. J., Koch, J., Smith, P. H., Hartogensis, O. K., De Bruin, H. A., et al. (2004). MATADOR 2002: A pilot field experiment on convective plumes and dust devils. *Journal of Geophysical Research*, *109*(E7). https://doi.org/10.1029/2003je002219

Richardson, M. I., Toigo, A. D., & Newman, C. E. (2007). PlanetWRF: A general purpose, local to global numerical model for planetary atmospheric and climate dynamics. *Journal of Geophysical Research*, *112*(E9). https://doi.org/10.1029/2006je002825

Sato, H., Kurita, K., & Baratoux, D. (2010). The formation of floor-fractured craters in Xanthe terra. *Icarus*, *207*(1), 248–264. https://doi.org/10.1016/j.icarus.2009.10.023

Senel, C. B. (2021). *JGRPlanets_Mars_CBL_Dust*. Open Science Framework, https://doi.org/10.17605/OSF.IO/MU6J8

Senel, C. B., Temel, O., Muñoz-Esparza, D., Parente, A., & van Beeck, J. (2020). Gray Zone partitioning functions and parameterization of turbulence fluxes in the convective atmospheric boundary layer. *Journal of Geophysical Research: Atmospheres*, *125*(22), e2020JD033581. https://doi.org/10.1029/2020jd033581

Senel, C. B., Temel, O., Porchetta, S., Muñoz-Esparza, D., & van Beeck, J. (2019). A new planetary boundary layer scheme based on LES: Application to the XPIA campaign. *Journal of Advances in Modeling Earth Systems*, *11*(8), 2655–2679. https://doi.org/10.1029/2018ms001580

Skamarock, W. C., Klemp, J. B., Dudhia, J., Gill, D. O., Barker, D. M., Duda, M. G., & Powers, J. G. (2008). *G.: A description of the advanced research WRF version 3 NCAR tech. Note NCAR/TN-475+ STR*. University Corporation for Atmospheric Research. https://doi.org/10.5065/D68S4MVH

Smith, D. E., Zuber, M. T., Frey, H. V., Garvin, J. B., Head, J. W., Muhleman, D. O., et al. (2001). Mars Orbiter Laser Altimeter: Experiment summary after the first year of global mapping of Mars. *Journal of Geophysical Research*, *106*(E10), 23689–23722. https://doi.org/10.1029/2000je001364

Smith, M. D., Wolff, M. J., Lemmon, M. T., Spanovich, N., Banfield, D., Budney, C. J., et al. (2004). First atmospheric science results from the Mars Exploration Rovers Mini-TES. *Science*, *306*(5702), 1750–1753. https://doi.org/10.1126/science.1104257

Spiga, A. (2019). The planetary boundary layer of Mars. *Oxford research encyclopedia of planetary science*. https://doi.org/10.1093/acrefore/9780190647926.013.130

Spiga, A., Barth, E., Gu, Z., Hoffmann, F., Ito, J., Jemmett-Smith, B., et al. (2016). Large-eddy simulations of dust devils and convective vortices. *Space Science Reviews*, *203*(1–4), 245–275. https://doi.org/10.1007/s11214-016-0284-x

Spiga, A., Faure, J., Madeleine, J.-B., Määttänen, A., & Forget, F. (2013). Rocket dust storms and detached dust layers in the Martian atmosphere. *Journal of Geophysical Research*, *118*(4), 746–767. https://doi.org/10.1002/jgre.20046

Spiga, A., & Forget, F. (2009). A new model to simulate the Martian mesoscale and microscale atmospheric circulation: Validation and first results. *Journal of Geophysical Research*, *114*(E2). https://doi.org/10.1029/2008je003242

Spiga, A., Forget, F., Lewis, S., & Hinson, D. (2010). Structure and dynamics of the convective boundary layer on Mars as inferred from large-eddy simulations and remote-sensing measurements. *Quarterly Journal of the Royal Meteorological Society: A Journal of the Atmospheric Sciences, Applied Meteorology and Physical Oceanography*, *136*(647), 414–428. https://doi.org/10.1002/qj.563

Spiga, A., & Lewis, S. R. (2010). Martian mesoscale and microscale wind variability of relevance for dust lifting. *MARS*, *5*, 146–158. https://doi.org/10.1555/mars.2010.0006

Stanzel, C., Pätzold, M., Greeley, R., Hauber, E., & Neukum, G. (2006). Dust devils on Mars observed by the high resolution stereo camera. *Geophysical Research Letters*, *33*(11). https://doi.org/10.1029/2006gl025816

Stull, R. B. (2012). *An introduction to boundary layer meteorology*. Springer Science & Business Media.

Sun, J., Mahrt, L., Banta, R. M., & Pichugina, Y. L. (2012). Turbulence regimes and turbulence intermittency in the stable boundary layer during CASES-99. *Journal of the Atmospheric Sciences*, *69*(1), 338–351. https://doi.org/10.1175/jas-d-11-082.1

Temel, O., Karatekin, Ö., Gloesener, E., Mischna, M. A., & van Beeck, J. (2019). Atmospheric transport of subsurface, sporadic, time-varying methane releases on Mars. *Icarus*, *325*, 39–54. https://doi.org/10.1016/j.icarus.2019.02.014

Temel, O., Senel, C. B., Porchetta, S., Muñoz-Esparza, D., Mischna, M. A., Van Hoolst, T., & Karatekin, Ö. (2020). Large eddy simulations of the Martian convective boundary layer: Towards developing a new planetary boundary layer scheme. *Atmospheric Research*, *250*, 105381.

Therry, G., & Lacarrère, P. (1983). Improving the eddy kinetic energy model for planetary boundary layer description. *Boundary-Layer Meteorology*, *25*(1), 63–88. https://doi.org/10.1007/bf00122098

Thomas, R. J., Potter-McIntyre, S. L., & Hynek, B. M. (2017). Large-scale fluid-deposited mineralization in Margaritifer Terra, Mars. *Geophysical Research Letters*, *44*(13), 6579–6588. https://doi.org/10.1002/2017gl073388

Toigo, A. D., Lee, C., Newman, C. E., & Richardson, M. I. (2012). The impact of resolution on the dynamics of the Martian global atmosphere: Varying resolution studies with the MarsWRF GCM. *Icarus*, *221*(1), 276–288. https://doi.org/10.1016/j.icarus.2012.07.020

Tyler, D., & Barnes, J. (2013). Mesoscale modeling of the circulation in the Gale crater region: An investigation into the complex forcing of convective boundary layer depths. *International Journal of Manufacturing Science and Engineering*, *8*, 58–77.

Vicente-Retortillo, Á., Martínez, G. M., Rennó, N. O., Lemmon, M. T., & de la Torre-Juárez, M. (2017). Determination of dust aerosol particle size at Gale crater using REMS UVS and Mastcam measurements. *Geophysical Research Letters*, *44*(8), 3502–3508.

Wang, C., Forget, F., Bertrand, T., Spiga, A., Millour, E., & Navarro, T. (2018). Parameterization of rocket dust storms on Mars in the LMD Martian GCM: Modeling details and validation. *Journal of Geophysical Research: Planets*, *123*(4), 982–1000. https://doi.org/10.1002/2017je005255

Whiteway, J., Komguem, L., Dickinson, C., Cook, C., Illnicki, M., Seabrook, J., et al. (2009). Mars water-ice clouds and precipitation. *Science*, *325*(5936), 68–70. https://doi.org/10.1126/science.1172344

Wilson, J. R., & Hamilton, K. (1996). Comprehensive model simulation of thermal tides in the Martian atmosphere. *Journal of the Atmospheric Sciences*, *53*(9), 1290–1326. https://doi.org/10.1175/1520-0469(1996)053<1290:cmsott>2.0.co;2

Wolff, M. J., Smith, M. D., Clancy, R., Spanovich, N., Whitney, B., Lemmon, M. T., et al. (2006). Constraints on dust aerosols from the Mars Exploration Rovers using MGS overflights and Mini-TES. *Journal of Geophysical Research*, *111*(E12). https://doi.org/10.1029/2006je002786

Wolkenberg, P., Giuranna, M., Grassi, D., Aronica, A., Aoki, S., Scaccabarozzi, D., & Saggin, B. (2018). Characterization of dust activity on Mars from my27 to my32 by PFS-MEX observations. *Icarus*, *310*, 32–47. https://doi.org/10.1016/j.icarus.2017.10.045

Wu, Z., Li, T., Zhang, X., Li, J., & Cui, J. (2020). Dust tides and rapid meridional motions in the Martian atmosphere during major dust storms. *Nature Communications*, *11*(1), 1–10. https://doi.org/10.1038/s41467-020-14510-x